TAMPEREEN TEKNILLINEN YLIOPISTO
TAMPERE UNIVERSITY OF TECHNOLOGY

HESSAM KALBASI SHIRVANI

DESIGN MODELING AND CONTROL OF AN EXPERIMENTAL CYLINDRICAL GRINDER

Master of Science thesis

Examiner: prof. Asko Ellman
Examiner and topic approved by the Faculty Council of the Faculty of Mechanical Engineering and Industrial Systems
on 3rd December 2014

ABSTRACT

Hessam Kalbasi Shirvani: Design modelling and control of an experimental cylindrical grinder
Tampere University of technology
Master of Science Thesis, 53 pages, 3 Appendix pages
December 2014
Master's Degree Programme in Machine Automation
Major: Mechatronics and Micromachines
Examiner: Professor Asko Ellman

Keywords: cylindrical grinding, design, chatter vibration, nonlinear friction

Nowadays machining in manufacturing industry has become more competitive and demanding than ever before. Grinding as one of the last stages in the manufacturing process has been the focus of the research studies in the field of manufacturing for quite some time. Grinding process compared to the other machining operations involves in low rates of material removal. The thermal, metallurgical, and mechanical phenomena coupled with the grinding process, make the contact dynamics unpredictable and complicated; hence the grinding wheel life and cycle times cannot be determined from any available standard tables and charts. This is due to the fact that, a large number of parameters are influencing each other in a grinding process. During a grinding process there are undesirable experiences that can be included as thermal effects, chatter vibration, rapid grinding wheel wear, etc. In order to overcome these problems associated with the grinding process a correct understanding of the involving factors in the process is of great significance.

This thesis work is focused on design and implementation of a bench scale plain type cylindrical grinding machine for grinding of the rolls in plunge and traverse cut in the laboratory environment. The servo controlled feed-drives and slide-way motions, which allow an efficient operation, are presented for each axis of the machine. Nonlinear friction effect as one of the major disturbances affecting the motion control systems is identified for the in-feed axis of the machine tool based on LuGre model. A novel method for grinding force estimation by monitoring of the thrust force in the infeed axis is presented based on the identified friction. The implementation of such an approach benefits the low cost compared to the common methods which use the dynamometer sensors for condition monitoring of the grinding process.

A traverse grinding cut model is presented in succeeding chapter to show how this type of vibration can give rise to the grinding force value and make it unstable. The stability analysis for demonstration of the stability boundaries is presented, and the time domain cutting force in tangential and normal directions are presented numerically. Further investigations need to be conducted to validate the stability results.

PREFACE

This M.Sc. thesis was conducted at the Department of Mechanical Engineering and Industrial Systems at Tampere University of Technology, Finland in partial fulfilment of the requirement for the Master of Science degree in Machine Automation. The thesis work is a part of Grinding Project (Grant No.: 310093) funded by the Academy of Finland.

First and foremost, it is my great pleasure to express my highest gratitude and appreciation to my supervisors Professor Asko Ellman, Dr. Veli-matti Järvenpää, and Dr. Lihong Yuan, and for giving me outstanding supervision during the project. This consistent support has allowed myself to develop my knowledge and has provided an optimal environment for research. I would like to thank all members of the Machine Dynamics Lab for providing a great environment to conduct research. Their assistance during the project had a tremendous impact on continuing to keep this research moving forward. Many thanks to laboratory engineer Jarmo Ruusila whom without his help the building of the test rig was not possible.

Last but not least, my most sincere thanks as always, to my parents for their strong encouragement, unconditional love and prayers. Thank you for supporting me every step of the way and for constantly being there for me. I am greatly indebted to you. This M.Sc. thesis is dedicated to my parents.

Tampere, December 2014

Hessam Kalbasi Shirvani

CONTENTS

LIST OF FIGURES

LIST OF TABLES

LIST OF SYMBOLS AND ABBREVIATIONS

AC	Alternative Current
CAD	Computer Aided Design
DC	Direct Current
DDE	Delay Differential Equation
DQF	Direct-to Quadrature Transformation
FE	Finite Element
FOC	Field Oriented Commutation
FPGA	Field Programmable Gate Array
FRF	Frequency Response Function
PID	Proportional Integral Derivative
PWM	Pulse Width Modulation
RT	Real Time
a	Depth of cut (µm=, 1µm=10^{-6}m)
A	Cross sectional area of the beam (m^2)
A_B	Cross sectional area of the ball screw in transverse axis (m^2)
b	Width of the grinding wheel (mm, 1mm=10^{-3}m)
c	Center distance between pulleys (mm, 1mm=10^{-3}m)
c_g	Grinding wheel damping (N.s/m)
c_w	Workpiece damping (Ns/m)
d	Diameter of the Euler-Bernoulli beam model (m)
d_B	Diameter of the ball screw in transverse axis (m)
d_{pulley}	Diameter of the driving pulley (mm, 1mm=10^{-3}m)
D_{pulley}	Diameter of the driven pulley (mm, 1mm=10^{-3}m)
D_s	Grinding wheel diameter (mm, 1mm=10^{-3}m)
E	Modulus of Elasticity for the Euler-Bernoulli beam model (GPa)
E_B	Modulus of Elasticity for the ball screw in transverse axis (GPa)
$e(W_1, v_i)$	Identification error function
F_0	The preload of the ball screw on the transverse axis (N)
ΔF	Friction force in presliding region (N)
f_B	The ball screw drive frequency (Hz)
F_{cut}	Cutting force on the transverse axis (N)
F_c	Coulomb friction force (N)
f_F	The main component of grinding force harmonic frequency (Hz)
F_f	Friction force (N)
$F_{friction}$	Friction force on the transverse axis (N)
F_g	Grinding force for power calculation (N)
$F_{grinding}$	Estimated grinding force (N)
f_i	The Eigenfrequency of the Euler-Bernoulli beam model beam (Hz)
F_{Load}	Load force on the transverse axis (N)
F_N	Normal grinding force (N)
F_s	Static friction force (N)
F_{ss}	Steady state friction force (N)
F_t	Thrust force of the motor in infeed direction (N)
F_T	Tangential grinding force (N)
g	Gravity (m/s^2)

I	Second moment of area for the Euler-Bernoulli beam model (m^4)
i_a	Current in the winding a (A)
i_b	Current in the winding b (A)
I_B	Second moment of area for the ball screw in transverse axis (m^4)
i_d	Quadrature current in the winding a (A)
I_f	Input current of the infeed axis motor (A)
i_q	Quadrature current in the winding b (A)
J	Objective function
J_B	Inertia of the ball screw in transverse axis (kgm^2)
J_m	Inertia of the motor in infeed axis (kgm^2)
J_{rotor}	Inertia of the servo motor in transverse axis (kgm^2)
J_{table}	Inertia of the transverse axis table (kgm^2)
J_{total}	Total inertia on transverse axis drive (kgm^2)
K_{ct}	Torsional rigidity of coupling (Nm/rad)
k_f	Motor force constant (N/A)
k_g	Grinding wheel stiffness (N/m)
K_m	Motor torque constant (Nm/A)
k_N	Contact stiffness (N/m)
K_v	Motor viscous friction coefficient (Nm/A)
k_w	Workpiece stiffness (N/m)
L	Length of the Euler-Bernoulli beam (m)
l_B	Length of the ball screw in transverse axis (m)
L_{belt}	Belt length (mm, $1mm=10^{-3}m$)
L_{ind}	Motor inductance (H)
m	Mass of the grinding wheel and joint (kg)
m_{table}	Mass of the transverse axis table (kg)
M	Mass of the grinding spindle beam model (kg)
M_g	Mass of the grinding wheel (kg)
M_t	Mass of the table (kg)
M_w	Mass of the workpiece (kg)
N	Total number of poles for all phases
N_m	Operational rotational speed of the transverse axis motor (rpm)
p	Pitch of the ball screw (mm, $1mm=10^{-3}m$)
p'	Pitch of the ball screw (rev/mm)
P_m	Grinding power (watts)
p_t	Pitch of the ball screw for transverse axis (mm, $1mm=10^{-3}m$)
q	Velocity fraction of the grinding wheel to workpiece
R	Motor resistance (Ω)
$R(s)$	The real part of characteristic equation
s	Longitudinal feed of the workpiece (mm/rev)
$S(s)$	The imaginary part of characteristic equation
S_f	Safety factor for load torque calculation
t_1	Acceleration/deceleration time for the transverse axis motion (s)
T_L	Load torque on the infeed axis (Nm)
T_{Load}	Load torque on the transverse axis (Nm)
T_m	Driving motor torque (Nm)
u_s	Grinding wheel peripheral speed (m/s)
u_w	Workpiece peripheral speed (m/min)
$u(x,t)$	Deflection of the beam (m, s)

v	Relative velocity of surfaces in contact (m/s)
V_a	Voltage in winding a (v)
V_b	Voltage in winding b (v)
V_d	Quadrature voltage in the winding a (v)
v_f	Infeed velocity (mm/s, 1mm/s=10^{-3}m/s)
v_g	Side feed velocity (m/s)
V_q	Quadrature voltage in the winding b (v)
v_s	Stribeck velocity (m/s)
W_1	Expected static parameter vector
x	Displacement along the beam (m)
Δx	Displacement in presliding region (mm, 1mm=10^{-3}m)
x_g	Displacement of the grinding wheel (m)
x_w	Displacement of the workpiece (m)
z	Average bristle deflection (m)
α	Overlap ratio
δ_d	Hysteresis shape factor
θ_D	Contact angle with the driven pulley (rad)
θ_d	Contact angle with the driving pulley (rad)
θ_m	Angular displacement of the rotor (rad)
θ_L	Angular displacement of the load (rad)
σ_0	Initial stiffness of the contact at velocity reversal (N/mm, 1N/mm=10^3N/m)
σ_1	Microdamping coefficient (Ns/mm, 1Ns/mm=10^3Ns/m)
σ_2	Viscous coefficient (N/mm, 1N/mm,=10^3N/m)
τ	Time delay (s)
τ_0	Shear strength of the material being grinded (Mpa)
τ_g	Time delay in grinding wheel (s)
τ_w	Time delay in the workpiece (s)
$\varphi_i(x)$	Mode shapes of the beam
ε	Total penetration (m)
ε_{nom}	Nominal penetration (m)
$\Delta\varepsilon$	Relative motion between the workpiece and grinding (m)
γ	Cutting ratio
η	Grinding spindle efficiency factor
ζ	Damping coefficient of a second order system (Ns/m)
λ	Support factor for the transverse axis
μ_0	Friction coefficient of preload nut on the transverse axis
μ	Friction coefficient between the normal and tangential cutting force
μ_L	Friction coefficient of sliding surface on the transverse axis
ρ	Density in the Euler-Bernoulli beam model (Kg/m^3)
ρ_B	Density of the ball screw drive in transverse axis (Kg/m^3)
ω	Frequency of the beam oscillation (rad/s)
ω_g	Rotational speed of the grinding wheel (rpm)
ω_m	Rotational speed of the rotor shaft of infeed axis motor (rad/s)
ω_n	Natural frequency of a second order system (rad/s)
ω_w	Rotational speed of the workpiece (rpm)

1. INTRODUCTION

Grinding in the primitive concept is probably one of the first cutting processes known to man. It is the process of removing metal by use of abrasives which are bonded to form a rotating wheel. When the moving abrasive particles contact the workpiece, they act as tiny cutting tools, each particle cutting a tiny chip from the workpiece.

Figure 1.1 shows the chip formation in grinding process. The grinding chip is produced by means of a single abrasive grain. Unlike single-point cutting, the grinding process has the following characteristics: (1) particles with irregular shapes and random distribution along the periphery of the wheel are used as abrasive grains, (2) the average rake angle of the grain is highly negative (see Figure 1.1), such as negative sixty degree or even lower, and (3) grinding speeds are very high, typically 30 m/s [1].

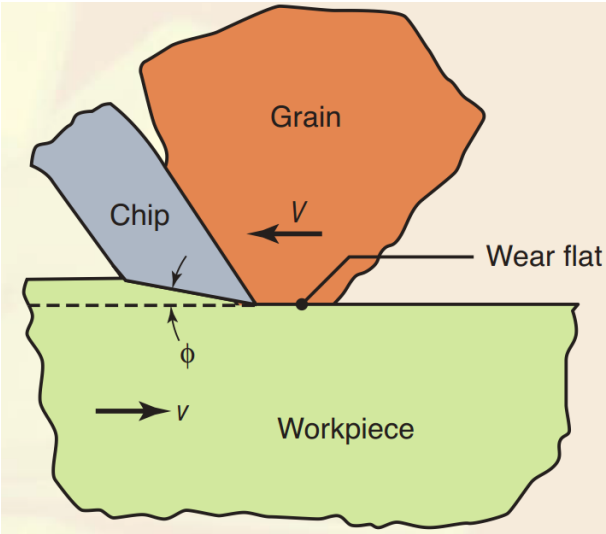

Figure 1.1 *Chip forming in grinding process [1]*

The specific grinding energy for a grinding process is consisted of three terms including, rubbing, ploughing, and cutting which describes the energy associated with each step of the process. The energy associated with the last stage of the grinding used for chip removal is considerably higher than the previous stages as it has been revealed [2]. The determination of grinding energy has a considerable practical significance since high energies give rise to high grinding forces, high temperatures, and rapid wheel wear as well poor work surface quality. The grinding specific energy is affected by wheel wear and wheel dressing conditions. Specific energy is also affected by wheel elasticity and wheel workpiece conformity [3].

1.1 Grinding machine

The grinding machine is used for roughing and finishing flat, cylindrical, and conical surfaces; finishing internal cylinders or bores; forming and sharpening cutting tools; and cleaning, polishing, and buffing surfaces.

Conventional grinding machines can be classified based on different types of surfaces that are being machined. The examples of four basic grinding operations are shown in the figure below.

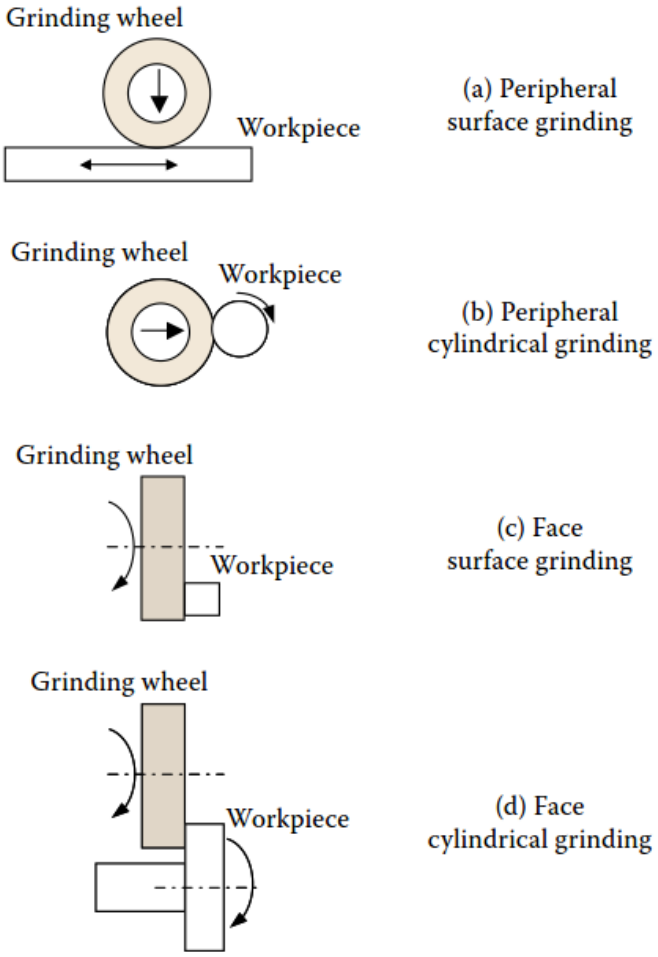

Figure 1.2 *Four basic grinding operations [4]*

The main feature of all these machines is the rotating abrasive tool which accomplishes the surface finish of the workpiece.

Cylindrical grinding machine is used to grind the external surface of cylindrical workpieces. The surface of the workpiece can be straight, tapered, with steps or profiled. Usually, the term cylindrical grinding refers to external cylindrical grinding process and the internal grinding is used for internal cylindrical grinding. Three types of cylindrical grinders are used as 1- Plain center type cylindrical grinding machine 2- Universal cylindrical surface grinder and 3- Centerless cylindrical surface grinding machine.

A cylindrical grinder shares many similarities with a center lathe machine. Since the workpiece set up between centers, held in a chuck and supported by a center rest, or clamped to a faceplate as in lathe setups. This type of cylindrical grinders can handle plunge grinding as well as traverse grinding processes. The parts that are normally handled with this type of machine include crankshaft bearings, spindles, shafts, pins, and rolls. In the cylindrical plunge grinding process the grinding wheel and the workpiece are the rotating axis while in the traverse cut there is the additional kinematic motion of the crossfeed which is the relative motion of the workpiece and the grinding wheel in the perpendicular direction to the plane of the wheel rotation.

A disc type grinding wheel carries out the grinding operation by its peripheral rotation and the infeed axis which feeds different depth of cut for the grinding process. Figure 1.3 is the demonstration of plain center type cylindrical grinder.

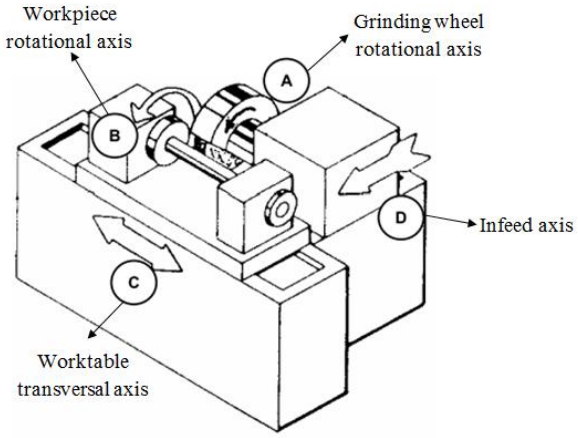

Figure 1.3 *A plain type cylindrical grinder*

The traverse and plunge grinding process for the plain center type grinder is shown in the figure above. In figure 1.3, and 1.4 axis (A) shows the rotation of the grinding wheel, (B) is the rotation of the workpiece, (C) shows the reciprocation of the worktable and finally the (D) axis is the infeed axis of the machine.

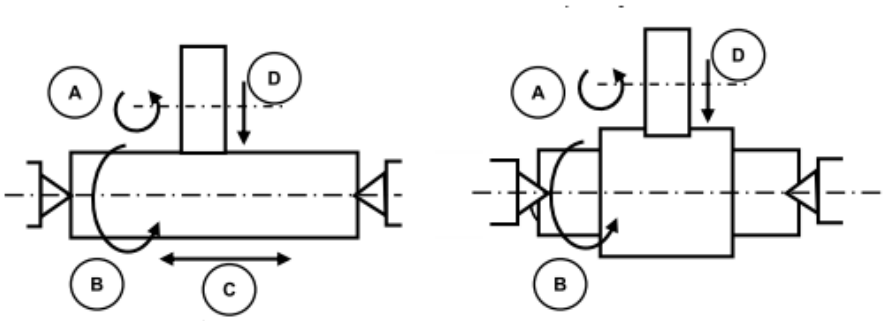

Figure 1.4 *Schematic illustration of traverse (left) and plunge grinding process (right)*

Plunge grinding is carried out in the shorter time compared to the traverse grinding process since the full wheel is engaged with the workpiece.

1.2 Motivation

Due to the complex nature of the grinding process and its contact dynamics it is strongly believed that contact problem description integrated with the dynamics of the vibration in cylindrical grinding can provide new scientific methodologies and solutions for the control of such undesired phenomenon in the machining. In order to achieve this goal and to investigate on the contact dynamics in grinding process a test rig capable of the machining of the products with specified dimensions needs to be constructed. Since the plain type cylindrical grinders are widely used in manufacturing of a variety of products in industry, this type of cylindrical grinder is opted for the study.

1.3 Thesis objectives and scope

In this study a test rig for performing cylindrical grinding process is developed. This development includes conceptual and detailed design of each axis, motion control software and hardware implementation and the communication protocols and interfaces, as well as physical construction of the machine structure. The physical implementation of the machine structure deals with the manufacturing and the assembly of the parts used for the construction.

The design of a cylindrical grinding machine similar to engine lathe machine, has to be carried out based on the wokpiece maximum diameter and length dimensions. The maximum dimensions of the workpiece that has been chosen for the plunge and traverse grinding process in this study has maximum diameter of 150 mm, and a maximum length of 200 mm. Based on the determined properties and dimensions of the workpiece the torque and velocity requirement for each axis of the machine is calculated. The rest of the thesis is organized as follows:

Chapter 2 presents the power calculation and transmission element requirements as well as the grinding spindle model for the test rig.

In chapter 3 the chatter vibration in a traverse grinding cut is studied and the stability analysis is performed.

Chapter 4 includes the calculations of the infeed axis of the machine tool. The friction identification and indirect cutting force measurement based on the infeed axis is presented through this chapter. Chapter 5 describes the considerations taken into account for the transverse movement of the workpiece. In chapter 6 the implementation of the rotational axis for the machine is explained. Finally, Chapter 7 appends some concluding remarks to the thesis.

2. GRINDING SPINDLE

The machine tool spindle is the most important part of each machine tool since it provides the relative motion between the tool and the workpiece and the torque needed to perform material removal. Hence, spindle specifications can greatly influence the machine tool overall performance and the surface quality of the workpiece. Spindles can be used as a condition monitoring and diagnostics tool for the machining process. The increasing use of sensors is not only a source of information for the machinist to optimize the cutting process and check the spindle health, but also allows the use of control techniques and actuators to avoid dynamic and thermal problems online [5].

2.1 Grinding power and torque requirement

One of the first steps that have to be taken in the design procedure of the cylindrical grinding machine is the calculation of power required for a certain metal removal rate. This has to be determined to choose the right motor for driving the spindle. Grinding data are seldom available in handbooks, which usually recommend a small range of depth, and work speeds at constant grinding wheel speed.

The determination of the amount of the available spindle power that can be utilized for chip removal under no chatter conditions at any given spindle speed is of great significant. The objective of this section is to predict the dynamic behavior of the spindle and multiple natural frequencies.

The grinding specific energy can be chosen according to the requirements for a specific grinding scenario. The movement of the grinding wheel is designed in such a way that provides grinding capability for cylindrical surfaces and planes perpendicular to the center line of the workpiece.

Grinding wheels vary enormously in design based on the application they are used. A grinding wheel is bonded and designed according to the particular process requirement. A general-purpose wheel will give greatly inferior removal rates and economics compared to an optimized and appropriate wheel for the particular product. However, wheel selection and optimization can be critical for large-scale production in aerospace and automotive industry. A larger diameter of the grinding wheel results in a longer wheel life, and moreover it eases the problem coupled with small diameters at high speeds which raise the risk of grinding wheel explosion.

The grinding wheel used in the presented test rig has a thickness of $25mm$, hole size of $51\ mm$ and the outer diameter of $200mm$ with electro bonded aluminum oxide in ceramic bonding and hardness grade of M. Based on the dimension of the grinding wheel and the workpiece the power and speed requirement is initially calculated for a direct drive.

Recommended grinding parameters are summarized in Table 2.1, and 2.2 for optimal selection of the grinding wheel, and workpiece speed, depth of cut, grit size, and specific material removal rate.

In the tables below parameter q denotes the fraction of the circumferential velocity of the grinding wheel to the workpiece, u_w is the circumferential speed of the workpiece in m/min, and finally u_s is the circumferential speed of the grinding wheel in m/s. The width of the grinding wheel is represented by b in mm. Parameter a shows the depth of cut in μm and s states the longitudinal feed of the workpiece in $mm/rotation$.

Table 2.1 *Standard values for grinding [6]*

Grinding	**Steel, soft Corundum**				**Steel, hard Corundum**				**Cast iron Silicon Carbide**				**Light metal Silicon carbide**			
	I	II	III	IV	I	II	III	IV	I	II	III	IV	I	II	III	IV
Grain size	54	36	36	22	54	40	36	22	54	36	36	22	54	40	36	22
Grade	M	L	L	K	K	I	K	I	L	K	L	I	I	H	I	H
u_s m/s	32	25	32	32	25	32	32	32	25	20	25	25	16	12	16	16
$q = \frac{60 \cdot u_s}{u_w}$	125	80	80	50	125	80	80	50	100	63	63	40	50	32	32	20
I external cylindrical grinding II Internal Cylindrical grinding III Surface grinding with the wheel circumference IV Surface grinding with the grinding face																

Table 2.2 *Depth of cut and feeds in grinding [6]*

Grinding method	**Rough grinding cut**	**Finish grinding**
Depth of cut a (µm)	20 … 50	2,5 …10
Longitudinal feed s (mm/rev)	(2/3 … 4/5)·b	(1/4 … 1/2)·b

The recommended grinding wheel speed normally has a range between $1200\ to\ 1800\ m/min$ and this value for the workpiece varies between$20\ to\ 40\ m/min$.

From Table 2.1 for an external cylindrical grinding process of hard steel we have the following values as

$$q = 125 \tag{2.1}$$

Based on the fraction value q and the maximum grinding wheel circumferential speed of 25 m/s the workpiece circumferential speed is determined as

$$u_w = 12\ m/min \tag{2.2}$$

$$s = \frac{4}{5} b = 20\ mm/rev \tag{2.3}$$

The grinding force for an external cylindrical grinding scenario with hard steel based on the values of the Tables 2.1, and 2.2 and the determined values is calculated as following

$$F_g = \tau_0 \frac{a \cdot s \cdot u_w}{u_s \cdot 60} \approx 7\,N \tag{2.4}$$

Where F_g is the external grinding force, $\tau_0$is the shear strength of the material being grinded in N/mm^2 (Steel 1 C cold worked $\tau_0 = 875.6\ Mpa$), and a is the depth of cut in mm. The maximum depth of cut of $50\ \mu m$ is chosen in the calculation of the cutting force to estimate the force for rough grinding case. By taking this value as the maximum depth of cut the resulting maximum power can be determined as

$$P_m = \frac{F_g \cdot u_s}{\eta} \approx 218.9\ Watts \tag{2.5}$$

Where P_m is the maximum power, η demonstrates the efficiency of the grinding spindle including the transmission element (belt). The standard transmission factor used for the belt driven spindle is 0.8. For the rotational speed of the grinding wheel we have

$$\omega_g = \frac{1000 \cdot u_s}{D_s \cdot \pi} \approx 2387\ rpm \tag{2.6}$$

Where ω_g is the rotational speed of the grinding wheel, and D_s is the diameter of the grinding wheel.

The driving motor torque at 100% load is calculated as follow

$$T_m = \frac{9550 \cdot P_m}{\omega_g} \approx 0.875\ N.m \tag{2.7}$$

where T_m is the motor torque

The motor that has been chosen to run the spindle is a K21 R 63 G2 three phase motor with squirrel cage rotor from VEM Company. The speed variation of the motor is carried out using a MI1 Vacon variable frequency drive.

The variable frequency drive alternating current is fed to the motor at a frequency and voltage required to produce the desired motor speed, and a $50\ Hz$ frequency produces 100% of the motor speed.

2.1.1 Power transmission

A belt-driven Spindle is quite similar in design to a conventional direct driven spindle, with some noticeable differences. A typical belt driven spindle assembly consists of the spindle shaft, held with a bearing support system. The mechanism that provides the force to run the grinding spindle is usually externally mounted. This means the power and rotation are supplied to this spindle by an external motor. The motor is mounted adjacent to the spindle, and the torque is transmitted to the spindle shaft by means of a cogged or v-belt. The power, torque and speed of the spindle will therefore depend upon the characteristics of the driving motor, and the belt ratio used between the motor and the spindle. The application of belt drive for the spindle makes it possible to have power, torque and speeds which are dependent upon the driving motor final specifications that can be modified based on the application by choosing a different motor or belt ratio. In this case high power and torques are possible to be applied since the driving motor is mounted externally to the spindle shaft. Therefore, it is often possible to use a very large motor for running the spindle. However, the application of belt driven spindle limits the maximum speed since it generates excessive vibration.

A v-belt drive is a non-synchronous drive that offers a very smooth rotating action with minimum vibration, and is suited for applications such as grinding or finish, and boring. A v-belt type drive for the spindle is designed to drive the grinding wheel. The driving pulley (SPZ 60) has an outer diameter of $60\ mm$ and the driven pulley (SPZ 562) on the spindle has an outer diameter of $110\ mm$ and with taper lock bushing on the shaft. So the transmission ratio of the belt drive is 0.545. Based on the maximum output speed of the motor $3100\ rpm$ the spindle can achieve the speeds up to $1690\ rpm$, which results in maximum circumferential speed of about $18\ m/s$ for the grinding wheel.

The center distance between pulleys is $c = 100\ mm$. For the calculation of the contact angles we have

$$\theta_d = \pi - 2\arcsin\left(\frac{D_{pulley} - d_{pulley}}{2c}\right) \approx 2.4619\,rad \tag{2.8}$$

$$\theta_D = \pi + 2\arcsin\left(\frac{D_{pulley} - d_{pulley}}{2c}\right) \approx 3.8213\,rad \tag{2.9}$$

In the above equations D_{pulley} describes the diameter of the driven pulley, d_{pulley} is the driving pulley diameter, θ_d, and θ_D are the contact angles for the driving and driven pulleys respectively.

The length of the belt can be obtained as [7]

$$L_{belt} = \sqrt{4c^2 - (D_{pulley} + d_{pulley})^2} + \frac{1}{2}\left(D_{pulley}\theta_D + d_{pulley}\theta_d\right) \approx 531\ mm \tag{2.10}$$

The belt tension is applied by the motor displacement to assure proper belt tension at all times. This ensures full power transmission from the motor. The proper belt tension eliminates too tight or too loose tension problems that may affect grinding quality. Figure 2.1 depicts the geometry of the power transmission system used in the machine.

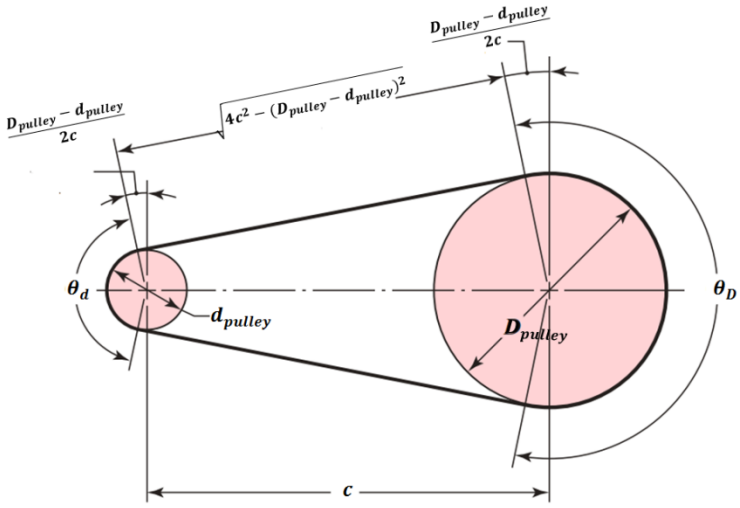

Figure 2.1 *Illustration of the belt-pulley transmission system*

2.2 Grinding spindle model

The complete Finite Element (FE) spindle model requires knowledge of the bearing preload, location, and the assembly tolerance for each component to define the stiffness. This data is not generally available in production environments. Furthermore, the model

damping cannot be predicted from first principles and requires tuning of the model by matching the spindle modes to a measured response. In addition, the complex FE models are often computationally expensive.

In this section the calculation of the numerical bending mode shapes for grinding spindle assembly is considered by using an Euler–Bernoulli beam with a mass at the end, which illustrates the mass related to the grinding wheel, flange, taper, bolt, as well as the locknut. Figure 2.2 is the demonstration of the model with the beam parameters.

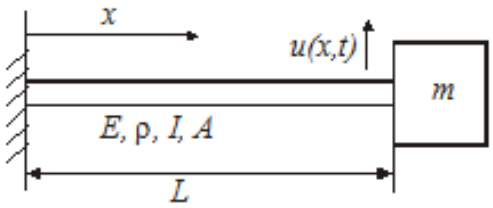

Figure 2.2 *Grinding wheel spindle assembly beam model*

M, ρ, A, L, E and I are the representation of the mass, density, cross sectional area, Young's Modulus, and moment of inertia, respectively. The parameter x shows the displacement along the beam with fixed condition at $x = 0$, and inertia (mass) at $x = L$. Parameter u shows the deflection of the beam and m is the mass on the tip of the beam.

The following partial differential equation below describes the uniform Euler-Bernoulli model for no loading condition.

$$M\frac{\partial^2 u}{\partial t^2} = -EI\frac{\partial^4 u}{\partial x^4} \tag{2.11}$$

Assuming that the independent variables can be separated, the deflection of the beam as a function of time and displacement can be stated as below

$$u(x,t) = \varphi(x)q(t) \tag{2.12}$$

This simplifies the partial differential equation into two ordinary differential equations. In the above equation $\varphi(x)$ shows the mode shape function, and $q(t)$ is the function of time and they are stated as follows

$$\varphi(x) = (c_1 \sin\beta x + c_2 \cos\beta x + c_3 \sinh\beta x + c_4 \cosh\beta x) \tag{2.13}$$

$$q(t) = (c_5 \sin\omega t + c_6 \cos\omega t) \tag{2.14}$$

Then by substituting the equations 2.13 and 2.13 into 2.12 we obtain

$$u(x,t) = (c_1 \sin\beta x + c_2 \cos\beta x + c_3 \sinh\beta x + c_4 \cosh\beta x)\cdot(c_5 \sin\omega t + c_6 \cos\omega t) \tag{2.15}$$

In the above equations for simplification β, ϑ are defined as $\beta = \sqrt{\frac{\omega}{\vartheta}}$, and $\vartheta = \sqrt{\frac{EI}{\rho A}}$.

The four boundary conditions for this case can be written as

Boundary condition at the left-hand endpoint $u(0,t)=0$ and $\frac{\partial}{\partial t}u(0,t)=0$

Boundary condition at the right-hand endpoint $m\frac{\partial^2}{\partial t^2}u(0,t)=EI\frac{\partial^3}{\partial t^3}u(L,t)$

Based on the boundary conditions the coefficients C_1, C_2, C_3 and C_4 are determined, and C_5, C_6 are determined from initial conditions. Once these coefficients are determined the mode shape functions for each Eigenfrequency can be given as

$$\varphi_i(x)=\sin(\beta_i x)-\sinh(\beta_i x)-\frac{\sin(\beta_i L)+\sinh(\beta_i L)}{\cos(\beta_i L)+\cosh(\beta_i L)}(\cos(\beta_i x)-\cosh(\beta_i x)) \quad (2.16)$$

In order to obtain the Eigenvalues we have the matrix below

$$\begin{bmatrix} 0 & 1 & 0 & 1 \\ \beta & 0 & \beta & 0 \\ -\beta^2 sin(\beta L) & -\beta^2 cos(\beta L) & \beta^2 sinh(\beta L) & \beta^2 cosh(\beta L) \\ -EI\beta^2 cos(\beta L)+m\omega^2 sin(\beta L) & EI\beta^2 sin(\beta L)+m\omega^2 cos(\beta L) & EI\beta^2 cosh(\beta L)+m\omega^2 sinh(\beta L) & EI\beta^2 sinh(\beta L)+m\omega^2 cosh(\beta L) \end{bmatrix}\begin{bmatrix} C_1 \\ C_2 \\ C_3 \\ C_4 \end{bmatrix}=\begin{bmatrix} 0 \\ 0 \\ 0 \\ 0 \end{bmatrix} \quad (2.17)$$

By calculating the det of the matrix and some simplifications we get

$$\beta L\frac{\sin(\beta L)\cosh(\beta L)-\cos(\beta L)\sinh(\beta L)}{1+\cos(\beta L)\cosh(\beta L)}=\frac{M}{m} \quad (2.18)$$

$$f(\beta)=\beta L\frac{\sin(\beta L)\cosh(\beta L)-\cos(\beta L)\sinh(\beta L)}{1+\cos(\beta L)\cosh(\beta L)} \quad (2.19)$$

$$g(\beta)=\frac{M}{m} \quad (2.20)$$

In order to determine each β value associated with a certain Eigenfrequency the functions $f(\beta)$ and $g(\beta)$ are set equal to each other.

Table 2.3 shows the numerical values used for the calculations.

Table 2.3 *Grinding wheel and shaft specification*

ρ Density (kg/m3)	***E* Modulus of elasticity (Gpa)**	***L* Shaft length (mm)**	***d*Shaft diameter (mm)**	***m* Grinding wheel + joint mass (kg)**
7870	*205*	*200*	*35*	*2.449*

Based on the geometrical properties presented in the table for the determination of moment of inertia and cross sectional area we have

$$I = \pi \frac{d^4}{64} = 7.613 \times 10^{-8}\, m^4 \tag{2.21}$$

$$A = \pi \frac{d^2}{4} = 9.781 \times 10^{-4}\, m^2 \tag{2.22}$$

The numerical calculations of the Eigenfrequencies and mode shapes for the spindle assembly model have been carried out in the MathCad software environment. The Eigenfrequencies of the model are obtained from the Figure 2.3 for the three lowest modes. Each value of β is identified based on the mentioned procedure. The solutions are the points where two functions $f(\beta)$ and $g(\beta)$ coincide.

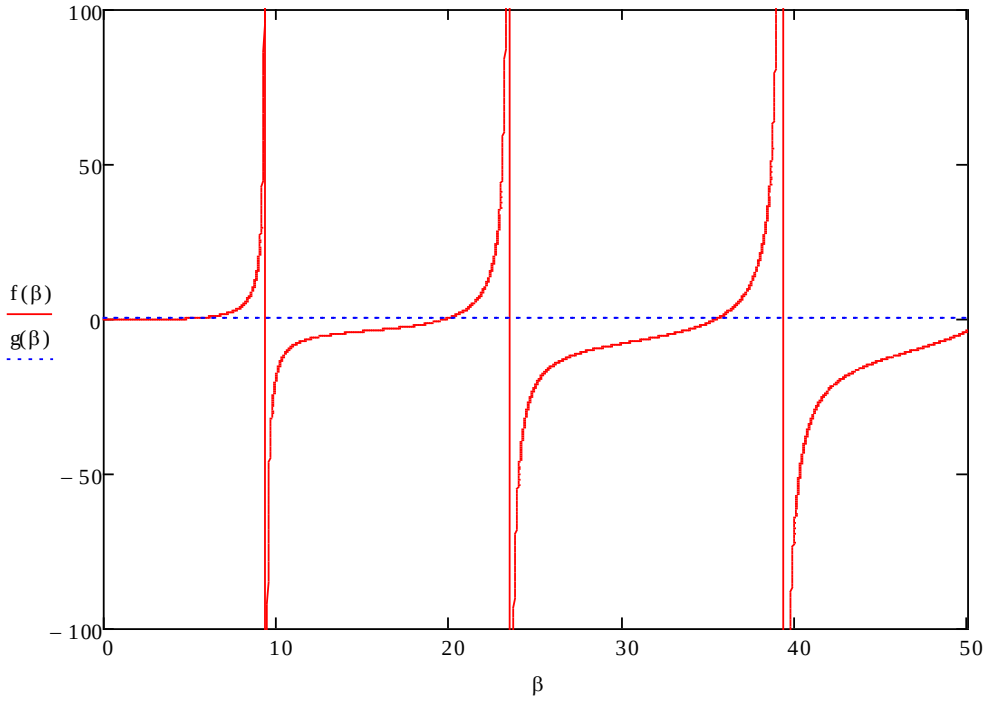

Figure 2.3 *Frequency curves for grinding wheel spindle model*

Based on the values determined for β in the previous section the frequency of the three lowest modes are calculated as

$$f_i = \frac{\beta_i^2 \vartheta}{2\pi},\ f = (227.2 \quad 2872 \quad 9052 \quad \ldots)^T Hz \ \ for\ i = 1, 2, 3, \ldots \tag{2.23}$$

Figure 2.4 is the demonstration of the normalized mode shapes for the three lowest Eigenmodes.

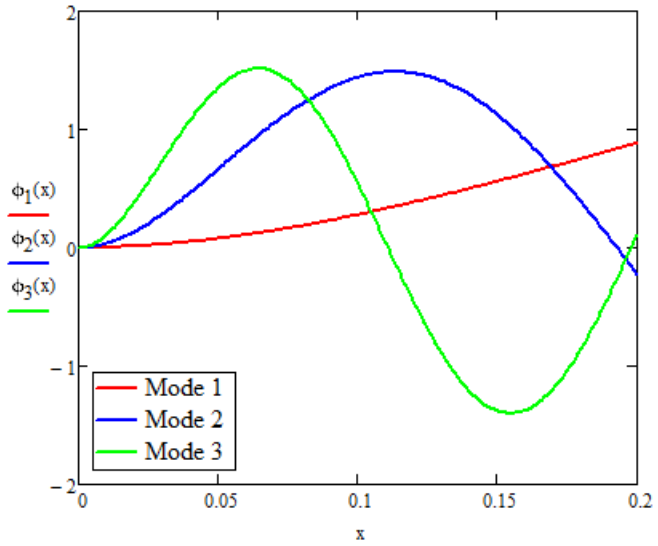

Figure 2.4 *Mode shapes for the three lowest modes*

This needs to be emphasized here that the calculated mode shapes of the assembly might not well describe the vibration mode of the spindle since the model only uses a concentrated mass at the end of the spindle shaft, and it does not capture the vibration mode associated with grinding wheel plate. This is due to the fact that the ratio of the grinding wheel diameter to thickness is large, and the rocking mode of the vibration has to be taken into account [8]. However the described model provides a good approximation of the Eigenfrequency for the grinding wheel assembly.

3. VIBRATIONS IN A GRINDING PROCESS

Generally the vibration in machine tools can consist of free vibrations, forced vibrations and self-excited vibrations based on the external energy sources. Free vibration in machine tools is referred to the vibrations that occur due to the impulsive and shocking loads. This can be as a result of inertia forces of parts in reciprocating motion (e.g. table motion reversal in grinding), or vibrations transmitted from the machine tool foundation. This type of vibration excites the natural frequencies of the machine structure and it decays at a rapid time. The second type of vibrations in machine tool is known as the forced vibration. It is generated by the periodic forces applied to the machine. These periodic forces can be due to the unbalanced rotating masses, misalignment of the machine elements, bearing defects, and etc. There are a few types of external forces that can create such a situation for the machine which includes harmonic, periodic but not harmonic, step, impulse and arbitrary force, etc. Self-excited type of vibration is generated due to the interaction of dynamics of chip removal process and structural dynamics of machine tool. The vibrations in a cylindrical grinding process can be classified based on the origin point of the vibration. Bending, sliding, torsion of grinding spindle or the workpiece, plate oscillation of grinding wheel, self-deformation of the workpiece, as well as the effects of grinding wheel joint conditions can be considered as the main sources in the grinding, and wokpiece unit. Other sources of vibration can be stated as dressing issue such as self-deformation of the dressing tool, or the ones which are the results of installation issues for the machine, unbalanced excitation, geometrical run outs, error due to transmission component (e.g. belt drive), over loading of the support bearings, and so on. In the following section the analysis of chatter vibration during a traverse grinding cut is presented and numerical results are shown.

3.1 Chatter vibration in cylindrical traverse grinding

The successful operation of grinding process is highly dependent on the working condition of spindle, free of chatter vibration, and without overloading of the support bearings [9]. Chatter and chatter free regions are seen depending on the selected grinding spindle, and the workpiece speed range. However, by selecting an axial depth of cut equal to or less than the critical axial depth of cut; chatter free cutting condition can be achieved.

Chatter effect as a self-excited vibration in machine tools contributes to undesired surface finish of the workpiece, and can deteriorate the surface quality. It can lead to uneven wear of the grinding wheel, and undesired irregularities on the surface of the work-

piece. This is due to the fact that variation of the grinding force excites the natural vibration modes of the machine tool. It is necessary to redress grinding wheel before it loses its efficient cutting ability. Therefore the process takes additional time and abrasive waste. Chatter arising in grinding operations can also be explained by the regenerative effect. Although, the wear of the wheel is necessary to expose new abrasive grits. It is also a source of the regenerative instabilities. The modelling of the dynamic variation in shape of both the workpiece and the grinding wheel results two time delay in the equation of motion of the system. Since most of the practical grinding processes are unstable, dynamic investigations should be extended after the onset of instability [10]. The chatter marks on the workpiece can be observed by short length partly visible as surface waves; however the long length waves can only be measured in most of the cases.

As stated earlier a specific feature of the grinding chatter compared to other machining processes is that the chatter phenomenon exists both on the grinding wheel, and the workpiece. This results in a more complicated chatter mechanism.

Spindle of the grinder can be considered as one of the main sources of vibration in cylindrical grinding, due to the power transmission elements, compliance in support bearings, as well as grinding wheel joints. This fact is of great importance since the grinding feeds are significantly lower than other machining processes and even the low vibrations from the transmission elements affect the surface quality.

It is a potential means to improve the surface quality through the optimal selection of spindle speed [11]. Method of chatter vibration surveillance in spindle, by changing the speed as the control command has been studied in the literature [12], [13]. A nonlinear dynamic model for paper roll grinding process is proposed with a proportional derivative (PD) controller to suppress the effect of chatter vibration. In this model only the interaction of the grinding wheel and the roll is considered based on the wear theory [14]. A similar approach is used to control the tangential vibration for a cylindrical grinder however the controller was not able to react to the tangential chatter vibrations [15].

Many studies on chatter analysis for cylindrical grinding have been conducted [16, 17, 18, 19, and 20] considering one or two time delays for the process. Here a discrete model with two time delays for the traverse grinding is used.

The dynamic model of the grinding wheel and workpiece interaction is illustrated in Figure 3.1. The model is a two-degree of freedom lumped-mass model with two displacement variables as x_w, $x_g$representing the displacements of the workpiece and grinding wheel respectively.

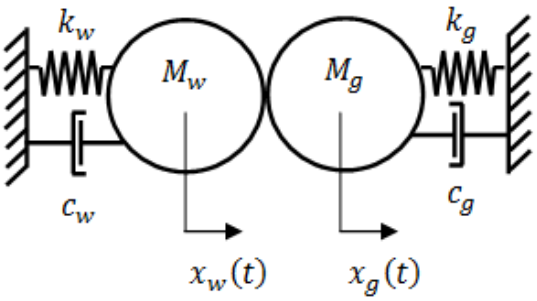

Figure 3.1 *Lumped-mass model of the grinding interaction*

Since there is a relative motion between grinding wheel and the workpiece in transverse movement and along the workpiece there is an overlap in the grinding of the area that has been machined in the previous round. The dynamic variation based on the relative motion of the workpiece and grindstone can be defined as

$$\Delta\varepsilon(t) = x_w(t) - x_g(t) \tag{3.1}$$

In the above equation $x_w(t)$, and $x_g(t)$ are the displacement in the workpiece and the grinding wheel respectively. For modelling of the grinding contact the time delay terms for both the grindstone and the workpiece is considered in the total penetration calculation. Total penetration with time delays in workpiece $\tau_w = \frac{2\pi}{\omega_w}$, and grindstone $\tau_g = \frac{2\pi}{\omega_g}$ is stated by the following equation [21]

$$\varepsilon(t) = \Delta\varepsilon(t - \tau_w) - \Delta\varepsilon\big(t - \tau_g\big) = \varepsilon_{nom} + \Delta\varepsilon(t) - \gamma\Delta\varepsilon(t - \tau_w) - (1 - \gamma)\Delta\varepsilon\big(t - \tau_g\big) \tag{3.2}$$

Where ω_w, and ω_g are the rotational speed of the workpiece, and grindstone respectively. In the case of cylindrical grinding $\tau_w > \tau_g$. It is due to the fact that the grindstone is normally running at higher speed compared to workpiece. In the above equation ε_{nom} denotes the nominal depth of cut which in the calculations is assumed to be zero.

Figure 3.2 shows the overlap in grinding path with overlap ratio α, and γ as the cutting ratio which indicates the elasticity of materials between the contact surfaces. In other words this parameter reflects the local compliance coefficient. The cutting ratio is close to unity in the calculations. When the workpiece fixture is assumed rigid the cutting ratio becomes as $\gamma = 1$. In the discussed model the error patterns due to the defects on the surface of the grinding wheel and the workpiece have been omitted in the penetration calculation. The grinding path is inclined due to the relative motion between the grindstone and the workpiece axial movement. The introduction of a constant overlap in the grinding path ensures that the surface will be ground evenly and consequently along the whole length.

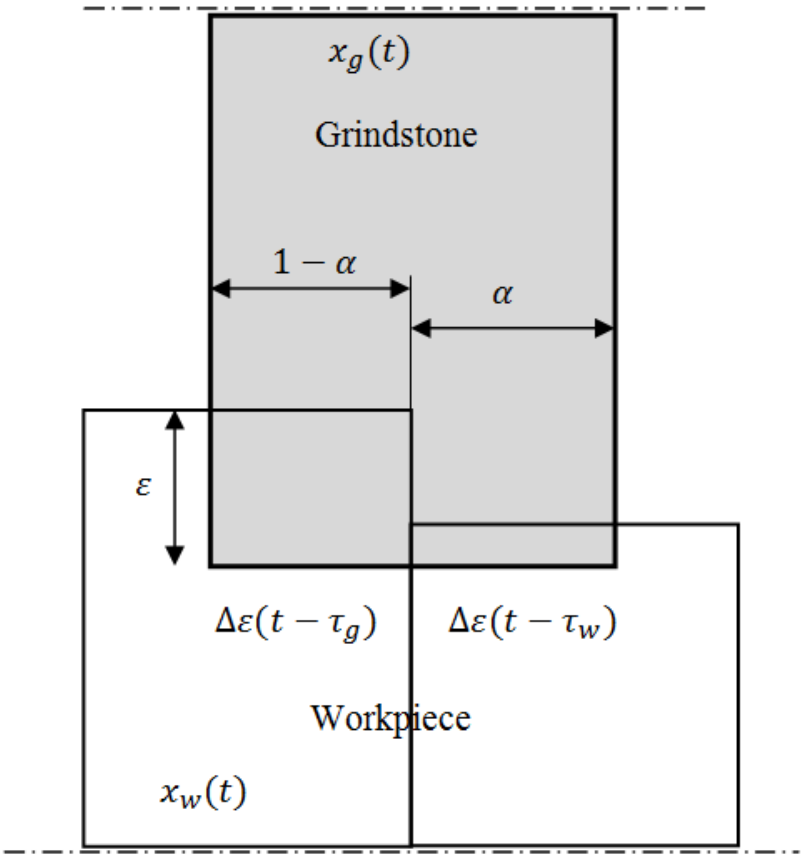

Figure 3.2 *Grinding contact [21]*

Substituting the total penetration with delay terms into the linear grinding force we get to the following equation where k_N represents the normal contact stiffness

$$F_N = k_N((1-\alpha)\varepsilon_{nom} + \Delta\varepsilon(t) - \alpha\gamma\Delta\varepsilon(t-\tau_w) - (1-\gamma)\Delta\varepsilon\big(t-\tau_g\big)) \quad (3.3)$$

In order to demonstrate the overlap ratio the equation below is used [22]:

$$\alpha = 1 - 2\pi\frac{v_g}{b\omega_w} \quad (3.4)$$

In the above equation v_g is the relative velocity between grinding wheel and the workpiece in side feed, and b denotes the width of the grindstone. The correlation between the normal F_N and tangential F_T components of the grinding force can be stated by means of a constant coefficient $\mu = \frac{F_T}{F_N}$ which describes the friction coefficient. By applying the Lagrange equation for the dynamic system we get the following equation

$$M_w\ddot{x}_w + c_w\dot{x}_w + k_w x_w = -F_N \quad (3.5)$$

$$M_g\ddot{x}_g + c_g\dot{x}_g + k_g x_g = F_N \quad (3.6)$$

The presence of time delay terms results in Delay Differential Equations (DDE), and the trajectories can uniquely be described in an infinite-dimensional phase space only. Since even in the case of a single degree of freedom system, the corresponding mathematical model is an infinite-dimensional one.

A stability chart determines the domains of the system parameter where the equilibrium is asymptotically stable. The stability limits can be stated in parameter space by plotting the so-called D curves. Taking a the simplest form of the DDE with one time delay into consideration as below

$$\dot{x}(t) = x(t-\tau) \tag{3.7}$$

where x is the state variable with $x \epsilon R$, and τ is the time delay term. By substitution of the trial solution $(t) = Ke^{st}$, K, $s \epsilon C$ the nontrivial solution for K can be obtained as

$$(s - e^{-s})Ke^{st} \rightarrow s - e^{-s} = 0 \tag{3.8}$$

which is the characteristic equation, and it has infinite number of solutions for the complex characteristic roots $s_i, i = 1,2, \dots$.

To study the grinding system stability, the Laplace transform of the dynamic model is determined when the initial conditions are zero.

$$\begin{Bmatrix} x_w \\ x_g \end{Bmatrix}(t) = \begin{Bmatrix} \hat{x}_w \\ \hat{x}_g \end{Bmatrix} e^{s_i t} \; or \; X(t) = \hat{x}_i e^{s_i t} \tag{3.9}$$

However, instead of considering the stability analysis for the system with all degrees of freedom we only consider the Equation 3.5 for the workpiece which gives enough good approximation of stable and unstable regions for the whole system as the time delay is larger in workpiece [23]. This plays an important role for determination of stability charts in the next stage. The characteristic equation when the nominal feed value is zero, and $x_g = 0$ becomes

$$D(s) = M_w s^2 + c_w s + k_w = -k_N(1 - Be^{-\tau_w s} - Ae^{-\tau_g s}) \tag{3.10}$$

where $B = \alpha\gamma$, and $A = (1-\gamma)$.

The complex valued roots of $s = a + ib$ can be solved to determine the system stable and unstable points. If the real parts of the roots are negative or all the roots lie on the left hand plane, the system is stable and on other hand the roots with positive real parts make the system unstable. Substituting $s = i\omega$, and by separation of the real $\boldsymbol{R(s)}$ and imaginary $S(s)$ parts of the equation we get

$$R(\omega) = Re\big(D(\omega)\big) = (-M_w\omega^2 + k_w + k_N) - k_N Bcos(\tau_w\omega) - k_N Acos(\tau_g\omega) \tag{3.11}$$

$$S(\omega) = Im\big(D(\omega)\big) = c_w\omega + k_N Bsin(\tau_w\omega) + k_N Asin(\tau_g\omega) \tag{3.12}$$

In order to obtain the D-curves for stability analysis, from the imaginary part of the equation, ω for each time delay is calculated numerically in MATLAB®, and then by use of real part of the equation the contact stiffness can be determined.

$$R(\omega) = 0, S(\omega) = 0, \omega\epsilon[0, \infty) \tag{3.13}$$

3.2 Stability charts

The stability charts for determination of cutting stiffness is investigated by taking two scenarios into account. In the first case the rotation speed of the workpiece is changed between 0.66 to 5 Hz and the grinding spindle is running at constant speed of 6.66 Hz. In order to capture the effect of overlap ratio in stability charts the stability charts are demonstrated for three different cases with 0.15, 0.20, and 0.25. In the second case rotation speed of the workpiece is fixed at 0.66 Hz, and the rotation speed in the grinding wheel is varied between 1 to 50 Hz. As the overlap ratio becomes higher the contact stiffness peak value in the period, tends to become lower. The cutting conditions in upper side of the curves will cause chatter, which is characterized by heavy vibration, tool damage, and poor surface quality. Figure 3.3 illustrates the two cases for the speed variation , and Figure 3.4 demonstrates the effect of overlap ratio on the shape of the stability curve.

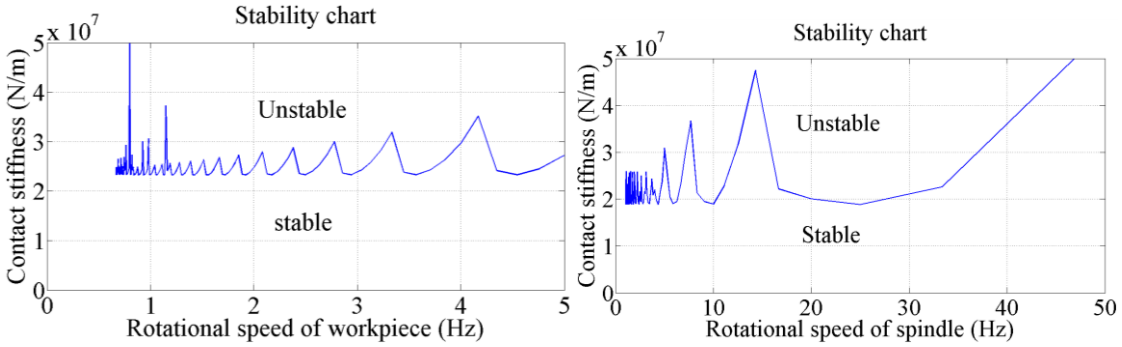

Figure 3.3 *Stability charts for spindle (right), and workpiece (left) with 15% overlap*

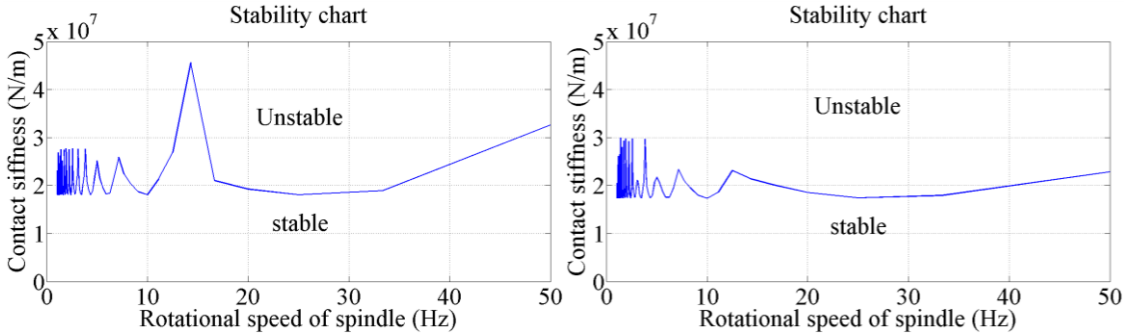

Figure 3.4 *Spindle stability charts for 20% (left) and 25% (right) overlap*

3.3 Numerical results

In order to observe the effect of the chatter vibration on the grinding force, the normal component of the grinding force in time domain is shown for two cases. In the first case a point in the stable region is chosen and the corresponding normal force is obtained; in the second case an unstable point from the stability chart is chosen as the selected point.

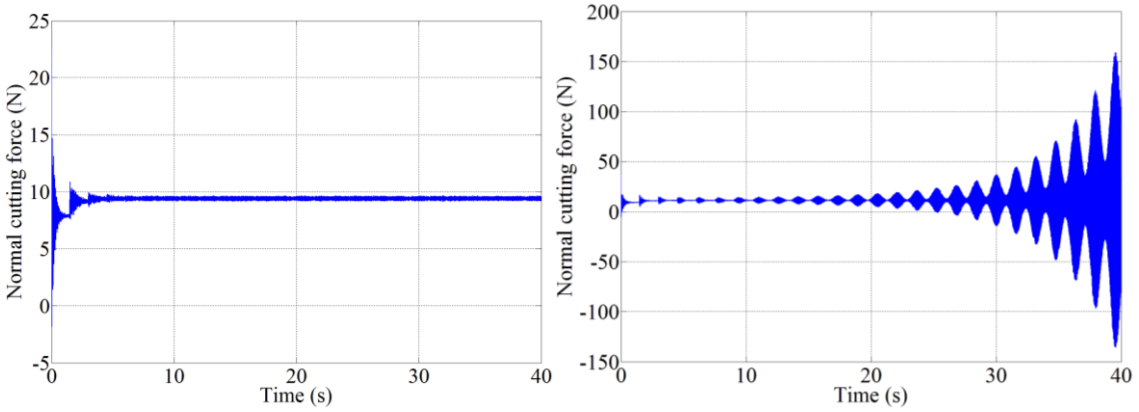

Figure 3.5 *The normal cutting force component: stable (left), and unstable (right)*

The time domain result for the grinding wheel axis is shown in the figure below. As it can be observed from the time domain response for the unstable case the displacement along x axis has been increased.

According to the stability charts, when spindle is running at 10 Hz, and the workpiece is running at 0.66 Hz, machine is in unstable situation with stiffness of $2.5\times10^7\,N/m$, and is stable with $1.5\times10^7\,N/m$. Figure 3.6 show the vibration of the spindle in x directions. The same overlap, and cutting ratio of 0.25, and 0.9 are used for both states. In Figure 3.5 the normal cutting force component is shown, and as it can be seen, the force value diverged during the period for the unstable case. The grinding forces were calculated for $2\ \mu m$ feed value. The same pattern exists in the grinding wheel response (see Figure 3.6).

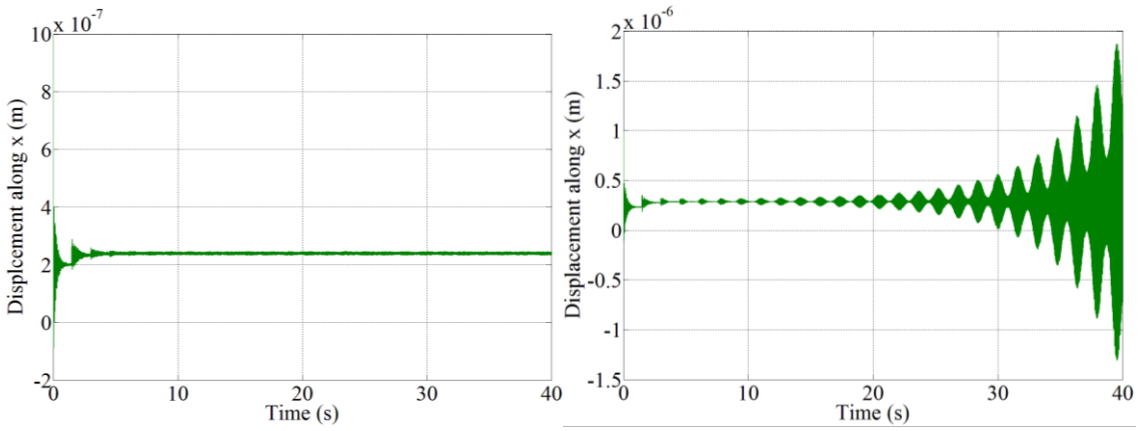

Figure 3.6 *The displacement of grinding wheel x-axis: stable (left), and unstable (right)*

4. INFEED AXIS

The infeed axis of a grinding machine controls the slide movement for grinding cycle by setting different feed rates for grinding. This movement and the rotational movement of the grinding wheel have to be performed to meet the required material removal rate. During the grinding process the infeed rate of the slide way is adapted in such a way that the resulting grinding force at the grinding wheel is perpendicular to the center line of the grinding spindle. Different types of the drives (Hydraulic, electrical motors) are used for the cylindrical grinders to drive the machine in infeed direction. Feed drives are used for positioning of the machine tool components carrying the cutting tool and the workpiece. Although pneumatic actuators exhibit less sensitivity to the temperature changes than hydraulic actuators, the nonlinearities due to air compressibility, friction effect and airflow through valve limit their applications in the field of machine tools [24, 25]. Ball screw drives are one of the most commonly used machine tool feed drives since they exhibit high efficiency, low wear, and heating behavior. The infeed motion of the machine is carried out using a ball screw driven actuator. The accuracy of the position measurement is highly depends on the accuracy of the ball screw drive. The accuracy depends also on the performance of the servo drive. As the cost of the drive control with hybrid stepper motors in servo performance is considerably lower than the other drives, and the risk of motor damage in the case of dirt, during the process is lower, this type of drive has been chosen for the infeed motion of the test rig. This type of drive also has another advantage over the other drives that is the data handling from the input to the drive motors is in digital form. It also benefits from better standstill stability, compared to the servo motors which resonate back and forth about the stopping axis. However the motor in stopped state suffers from the addition heating at the standstill state. The standstill properties of the motor are of great importance during the spark out stage where the motion is balanced with the friction characteristic of the feed drive. The motor that has been used for infeed axis is an EMMS-ST-42 from Festo Company which has a step angle of 1.8° and a holding torque of $0.5\ N.m$. The ball screw drive for the infeed axis is from EGC-70 series manufactured by Festo Company that has a maximum stoke length of $100\ mm$ and $10\ mm$ pitch. The minimum increment of the displacement that can be achieved with the drive is $0.01\ mm$. The motor is directly connected to the ball screw without any transmission elements. Figure 4.1 shows the ball screw actuator and its cross sectional view for the infeed axis.

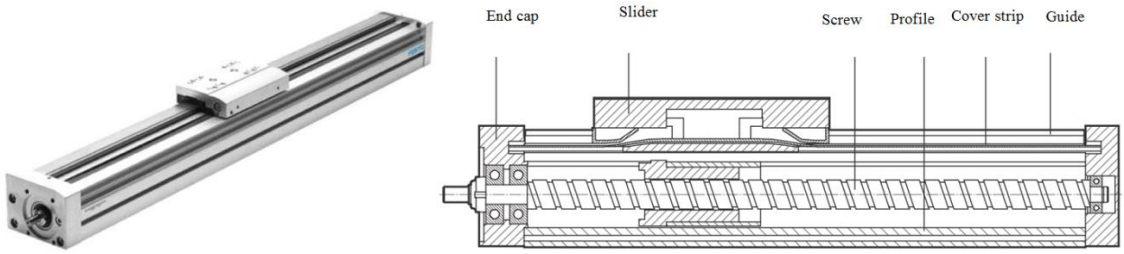

Figure 4.1 *Ball screw actuator and the sectional view for the infeed axis [26]*

The CMMO controller for the control of the infeed axis is used from the Festo Company which is capable of controlling of the axis in positioning, speed, and force control modes with (Proportional Integral Derivative) PID controller through FCT tool software.

Figure 4.2 *EMMS-ST-42Hybrid servo motor and the CMMO-ST controller [26].*

The linear motion guide ways are widely used in machine tools because of the high precision and accuracy as well as rigidity, and low friction coefficient. Application of the linear motion guides reduces the driving force needed for movement of the table. Due to the low frictional resistance the temperature rising effect is small in this kind of guides. Two TRH 20 FN linear guides with maximum dynamic and static load of $20.5\ kN$, and $36.96\ kN$ respectively are used on both sides of the grinding tool table for a smooth movement of this axis.

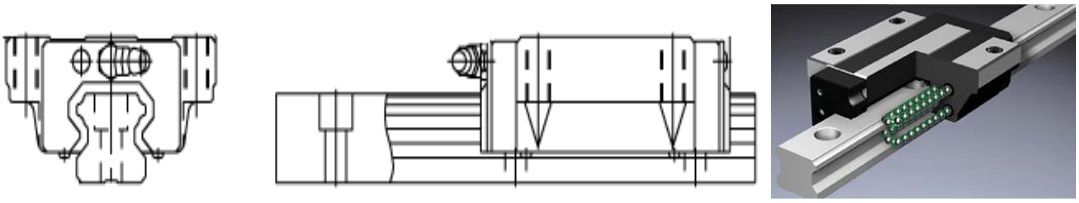

Figure 4.3*TRH 20FN Linear motion guide [27]*

Figure 4.4 shows the implementation of the linear guide in the test plan.

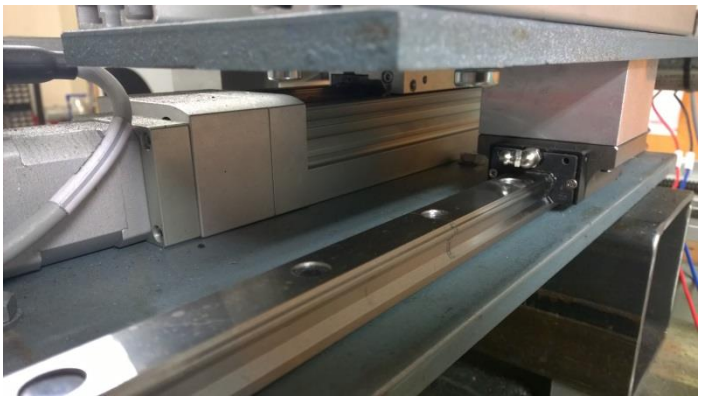

Figure 4.4 *Implementation of the linear bearing in the infeed axis of the grinding*

The CAD model of linear bearing implementation in the infeed axis is illustrated in the Figure 4.5.

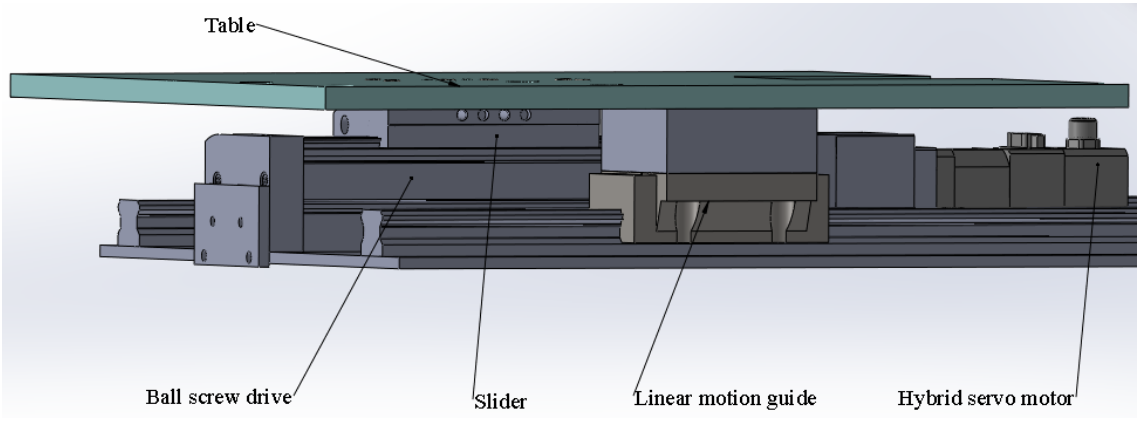

Figure 4.5*The layout of the linear bearings in the infeed axis of the test rig*

In order to describe the relationship between the motor phase current signals and the resulting thrust force of the drive, the modelling of the hybrid servo motor of the infeed axis is presented in the next section.

4.1 Modelling of Hybrid Servo Motor

The hybrid stepper motors are the combination of both permanent magnet and variable reluctance stepper motors. Similar to variable reluctance stepper motor, this type of motor is multi-toothed and contains an axially magnetized concentric magnet around the rotor shaft. For the 2-phase hybrid stepper motor with sinusoidal current impressing we have.

The rotor shaft dynamics is given by the following set of equations.

$$\frac{di_a}{dt} = \frac{1}{L_{ind}}(V_a - Ri_a + K_m\omega_m \sin(N\theta_m)) \tag{4.1}$$

$$\frac{di_b}{dt} = \frac{1}{L_{ind}}(V_b - Ri_b - K_m\omega_m \cos(N\theta_m)) \tag{4.2}$$

$$\frac{d\omega_m}{dt} = \frac{K_m}{J_m}\{-i_a \sin(N\theta_m) + i_b \cos(N\theta_m) - K_v\omega_m - T_L\} \tag{4.3}$$

$$\frac{d\theta_m}{dt} = \omega_m \tag{4.4}$$

$$T_{Thrust} = -K_m i_a \, sin(N\theta_m) + K_m i_b \omega \, cos(N\theta_m) - K_v\omega \tag{4.5}$$

In the above equations i_a , i_b are the currents through the windings of the motor, and V_a , V_b are the voltages in the winding a, and b. L , and R are the inductance and resistance of the motor, J_m , ω_m , and θ_m are motor inertia, rotational speed and displacement. N is the total number of poles for all phases together and K_m, K_v are the motor torque constant and viscous friction. T_{Thrust} is the thrust force of the motor.

In order to remove the trigonometric terms from the equations the Direct-to Quadrature Transformation (DQF) can be used to reduce the presence of high nonlinearity.

$$\left.\begin{matrix} [i_d, i_q]^T = M_p[i_a, i_b]^T \\ [v_d, v_q]^T = M_p[v_a, v_b]^T \end{matrix}\right\}, M_p = \begin{pmatrix} cos(N\theta_m) & sin(N\theta_m) \\ -sin(N\theta_m) & cos(N\theta_m) \end{pmatrix}, \tag{4.6}$$

Where i_d is the direct current, i_q, is the quadrature current, $v_d$is the direct voltage, and $v_q$is the quadrature voltage. Considering the above simplification and the case when the load is connected to the motor through a long stiff shaft with stiffness K_{ct} the model becomes as followings:

$$\frac{di_d}{dt} = \frac{1}{L_{ind}}(V_d - Ri_d + NL_{ind}\omega_m i_q) \tag{4.7}$$

$$\frac{di_q}{dt} = \frac{1}{L_{ind}}(V_q - Ri_q + NL_{ind}\omega_m i_d - K_m\omega_m) \tag{4.8}$$

$$\frac{d\omega_m}{dt} = \frac{1}{J_m}(K_m i_q - K_v\omega_m - T_L - K_{ct}(\theta_m - \theta_L)) \tag{4.9}$$

$$\frac{d\theta_m}{dt} = \omega_m \tag{4.10}$$

Where T_L , and θ_L are the load torque and rotational displacement.

The influence of the torsional deformation of the screw on the linear displacement of worktable can be ignored compared to the flexibility of the torsional deformation of the coupling and the axial deformation of the screw. With this in mind the torsional stiffness K_{ct} can be approximated as the torsional rigidity of the coupling.

4.2 Friction effect

Friction is inevitable, and exists in almost all motion control systems, and can contribute to tracking errors, and undesired stick-slip motion. Precise modeling, identification, and compensation of this phenomenon in grinding, is of great importance since it directly affects the surface finish of the final product.

The friction exists not only in the sliding contact of the ball screw drive but also in the bearing. However the bearings exhibit typically less friction than sliding contact. Friction is also present between the nut and the ball screw and since the drive is preloaded the amount of friction at this point is considerable. Brushless motors do not have commutator brushes, so this source of friction is omitted. Stepper motors are technically "brushless" and have high torque constants due to their electromagnetic gearing and can often be used without additional transmission gears so that the friction due to the transmission element does not exist in the drive, since the ball screw is directly driven by the motor. Despite the minimal mechanical friction as mentioned, the stepper motors do exhibit a significant nonlinear magnetic damping. So they do not act frictionless [28].

4.3 Dahl friction model

The Dahl model [29] is used extensively for simulating friction behavior in ball-bearing system. The model is an extension to the classic Coulomb friction, with smooth transitions around the critical zero velocity regions. This friction model is a generalized first order differential equation of the position that is a function of the sign of the velocity v, approximates the hysteresis at presliding regime. The function is describes below:

$$\frac{dF_f}{dx} = \sigma_0 \left| 1 - \frac{F_f}{F_c} \operatorname{sgn}(v) \right|^{\delta_d} \operatorname{sgn}(1 - \frac{F_f}{F_c} \operatorname{sgn}(v)) \tag{4.11}$$

F_f, and F_c are the total friction force and the Coulomb friction force respectively, σ_0 is the initial stiffness of the contact at velocity reversal, and δ_d determines the shape of the hysteresis. The above equation in its simplest form is as follows

$$\frac{dF_f}{dx} = \sigma_0 \left(1 - \frac{F_f}{F_c} \operatorname{sgn}(v) \right) \tag{4.12}$$

4.4 LuGre friction model

Among all the proposed friction models, LuGre model [30] captures most of the friction behavior that has been observed experimentally, which includes the Stribeck effect, hysteresis, as well as spring-like characteristics for stiction, and varying break-away force. This model is widely used in servo systems for friction compensation and to improve tracking error. The model is based on the average deflection bristles which are attached to rigid solids. These bristles as shown in Figure 4.5 demonstrate the asperity contact.

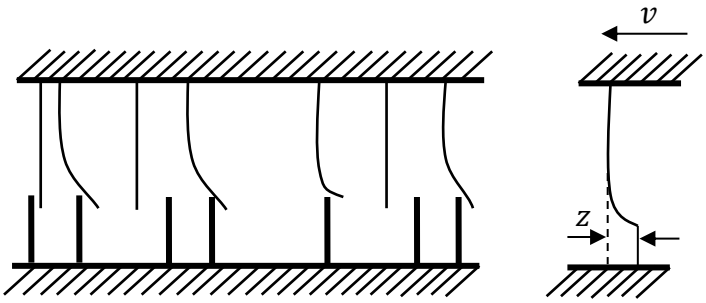

Figure 4.6. *Contact between bristles [30]*

Average bristle deflection z is defined by the following non-linear differential equation [30].

$$\frac{dz}{dt} = v - \frac{|v|}{g(v)} z \tag{4.13}$$

Friction force

$$F_f = \sigma_0 z + \sigma_1 \frac{dz}{dt} + \sigma_2 v \tag{4.14}$$

where v is the relative velocity between two surfaces in contact, σ_0 is bristle stiffness, σ_1 is microdamping coefficient and σ_2 is viscous coefficient. Stribeck effect that observes the transition of friction from static value to dynamic and then to viscous state, is described by the equation below

$$g(v) = F_c + (F_s - F_c) e^{-\left(\frac{v}{v_s}\right)^2} \tag{4.15}$$

where F_c is the Coulomb friction level, F_s is the level of stiction force, and v_s represents the Stribeck velocity. The friction force in steady-state for constant velocity is given by

$$F_{ss}(v) = g(v)\, sgn(v) + \sigma_2 v \tag{4.16}$$

The model reduces to the Dahl model [31] if $g(v) = \frac{F_c}{\sigma_0}$ and microdamping, and viscous friction are equal to zero. From the equations (4.13), and (4.14) we have

$$\frac{dF_f}{dt} = \sigma_0 \frac{dz}{dt} = \sigma_0 (1 - \frac{F_f}{F_c} \operatorname{sgn}(v)) \tag{4.17}$$

However, the Dahl's model does not describe the Stribeck effect and only accounts for Coulomb friction. Figure 4.6 shows the difference in the friction force relationship versus the velocity for Dahl and LuGre models.

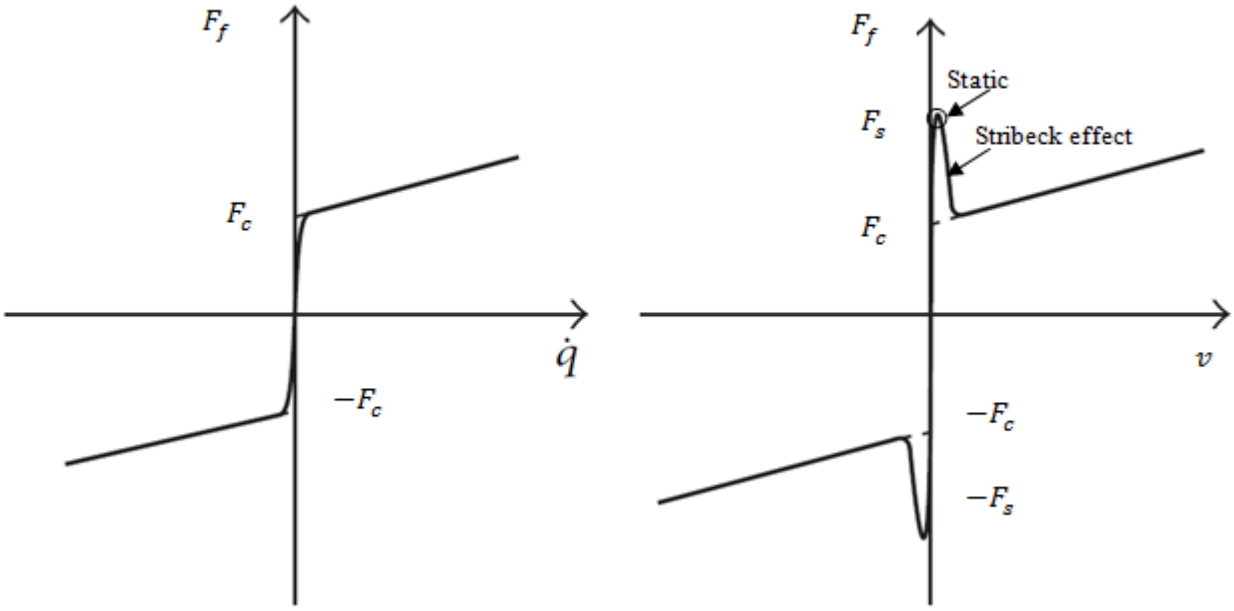

Figure 4.7. *Friction force versus velocity for Dahl (left) and LuGre model (right)*

Identification of the friction model for the in-feed axis can be divided into two steps. In the first step the static parameters of the model are estimated by means of Stribeck curve. Secondly the dynamic parameters are identified based on the spring like behavior of the drive in presliding region. In our in-feed axis the main source of friction elements are due to the 1- ball screw and nut interaction for transmission of the rotary motion to translational 2- linear bearings which are used to guide the worktable of the grinding machine and the other elements can be motor losses and preloaded bearings [32].

4.4.1 Static parameters identification

For the steady state motion when $\frac{dz}{dt} = 0$ the friction force can be calculated based on the equation (4.16), which means when the velocity is kept constant and there is not any other loading on the system, the friction force becomes as follow

$$F_f = k_f I_f = F_t \tag{4.18}$$

Where I is the input, k_f is the motor force constant, and F_t is the thrust force. When the I is held constant, velocity reaches the steady state, and the steady state friction force can be measured by repeating the experiment for different velocities. Figure 4.7 shows the measurement signals for 12 mm/sec velocity of the slide. In the upper part of the figure the current signal is measure in mA and the corresponding thrust force of the axis is stated in percentage of the total force. In the lower part of the graph the position signal for the axis which demonstrates the indirect measurement of linear movement from the rotary encoder plus the velocity measurement signal is shown.

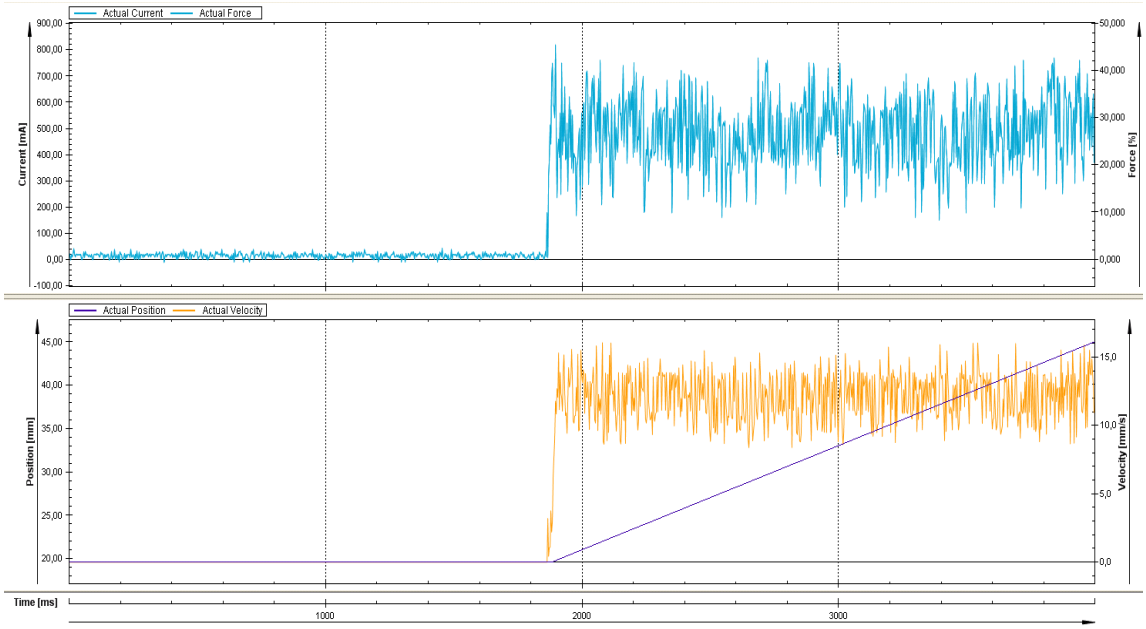

Figure 4.8 *Sample measurement of the thrust force for the steady-state velocity*

Figure 4.9 shows the Stribeck curve for velocity range up to 16 mm/sec of the worktable by means of subsequent measurement. By measuring the thrust force of the motor, the effect of preload on the ball screw for elimination of the backlash is observed besides the sliding friction. In order to achieve reliable results the thrust force has been measured at constant temperature for each velocity.

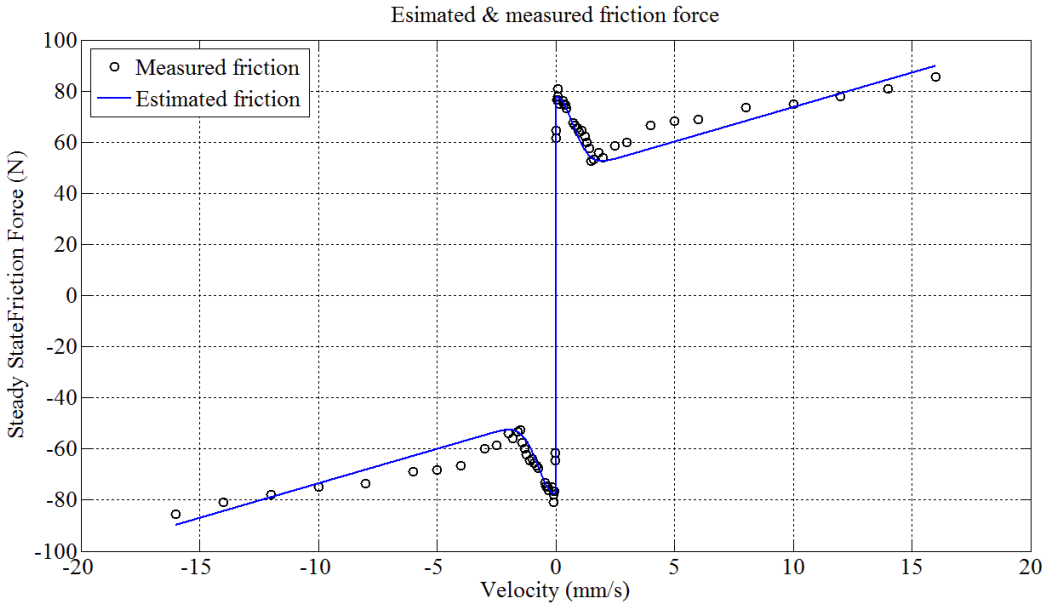

Figure 4.9. *Stribeck curve*

In order to identify the static parameters from the Stribeck curve we consider the equation 4.16 which demonstrates the axis behavior in steady state. Then by substituting $g(v)$ from the equation 4.15 into 4.16 we obtain the steady state behavior with four parameters as F_c, F_s, v_s, σ_2. Now let's assume a group of invariable velocities$\{v_i\}_{i=1}^{N}$, and the corresponding sequences of the control input are $\{u_i\}_{i=1}^{N}$ which is equal to axial force when $\dot{v} = 0$. Now suppose the expected static parameters as the following vector:

$$W_1 = [\hat{F}_C, \hat{F}_s, \hat{v}_s, \hat{\sigma}_2] \tag{4.19}$$

The identification error is defined as:

$$e(W_1, v_i) = F_{Ti}(t_i) - F_{ss}(w_1, v_i) \tag{4.20}$$

Where $F_{ss}(w_1, v_i)$ is the expected friction force. By taking the objective function as follows

$$J = \frac{1}{2}\sum_{i=1}^{N} e^2(W_1, v_i) \tag{4.21}$$

Then identification means to minimize the above objective function.

Identification of the static parameters is carried out by using a non-linear unconstrained optimization with the Nelder–Mead Downhill Simplex Algorithm in Matlab. This algorithm has the major advantage of short running time and does not require derivatives. It converges very rapidly when it finds a minimum. By using Nelder-Mead algorithm for determination of static parameters we obtain the values as stated in table below

Table 4.1 *Identified static parameters*

F_c (N)	F_s (N)	σ_2 (N.s/mm)	v_s (mm/s)
46.59	77.58	2.700	1.007

4.4.2 Dynamic parameters identification

The presliding regime is specified by small junction deformation where the internal friction state is immeasurable$|z| \ll g(v)$. And equation (4.13) reduces to $\frac{dz}{dt} = v$. The main problem with the presliding regime analysis arises from the correct initialization of the internal state variable z.

In order to identify the dynamic model parameters the frequency domain identification for frictional presliding behavior can be implemented. The identification procedure for the dynamic model parameters, i.e., 1) the stiffness and 2) the damping of the presliding phenomenon, is reduced from performing several dedicated experiments to one experiment where the system is excited with random noise, and the Frequency Response Function (FRF) of the phenomenon is measured [33]. In this study for determination of the dynamic parameters it is assumed that when an external force is applied the worktable does not move visibly. In this case $z \approx x$ and the system is represented by

$$M_t\ddot{x} + (\sigma_1 + \sigma_2)\dot{x} + \sigma_0 x = K_f I \tag{4.22}$$

Where M_t is the mass of the worktable. By taking the Laplace transform we get

$$\frac{x(s)}{I(s)} = \frac{k_f}{M_t s^2 + (\sigma_1 + \sigma_2)s + \sigma_0} \tag{4.23}$$

Equation 4.23 shows a damped second order system. In this state by taking the linear approximation [34] into account we have

$$\sigma_0 \approx \frac{\Delta F}{\Delta x} \tag{4.24}$$

Where ΔF, Δx are the force and displacement in presliding region. This deflection appears in the start, and stop situation at the time of speed change. In order to create such a condition we let the drive do a short-stroke reciprocating motion with a low speed of $0.5\ \mathrm{mm/s}$. The displacement of the worktable is measured by using the indirect measurement where the rotary encoder which is attached to the motor drive is used. The optical encoder has $500\ \mathrm{pulse/rev}$.

It is important to filter both input, and output signals before starting identifying, otherwise the filter dynamic will be included in the resulting system. Filtering a signal introduces a delay that can distort the signal. This delay can be constant over all frequencies or it can be frequency dependent and contribute to phase distortion. In or to implement zero-phase filtering of the data the filtfilt function in Signal Processing Toolbox of MATLAB has been used [35], and the result has been compared with the case when no delay compensation is implemented. Figure 4.9 is the demonstration of original and filtered signal for the two cases. The filtering is carried out by means of a 5th order Infinite Impulse Response (IIR) lowpass filter with cut-off frequency of 20 Hz. The group delay of the filter is frequency dependent.

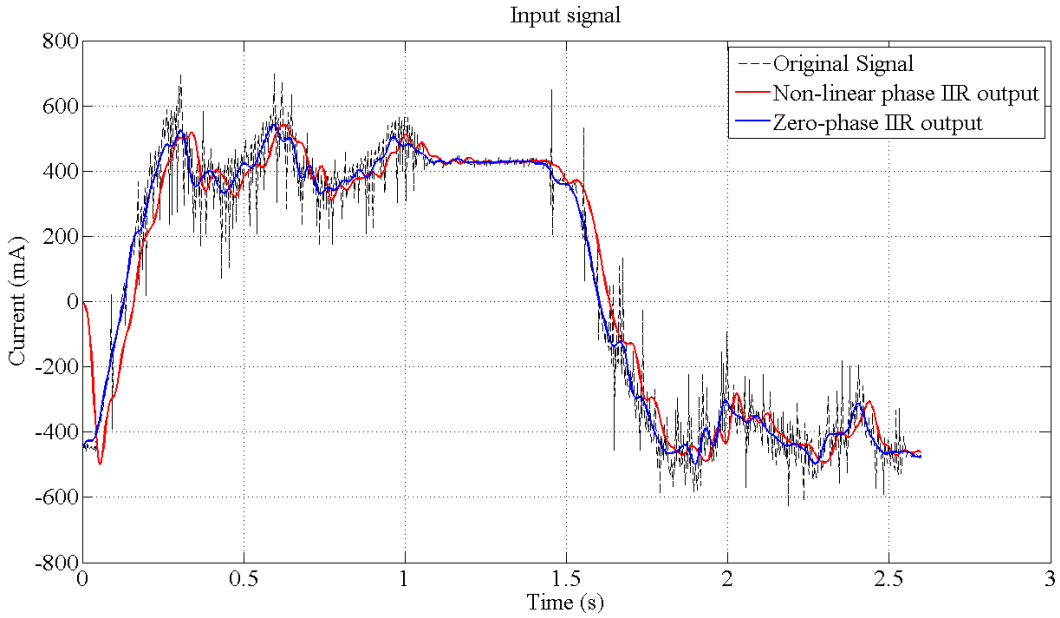

Figure 4.10. *Input signal filtering with and without delay compensation*

As it can be observed from the Figure 4.10 the spring-like phenomenon appears at the presliding region [0 50 µm] and from there we can get σ_0 as $1.358 \times 10^3 N/mm$. As it was mentioned the system in this case can be considered as a second order damped system as $s^2 + 2\xi\omega_n s + \omega_n^2$ where $\omega_n = \sqrt{\dfrac{\sigma_0}{M_t}}$ is the natural frequency and $\xi = \dfrac{\sigma_1 + \sigma_2}{2\sqrt{M_t \sigma_0}}$ denotes the damping coefficient.

In this case for microdamping term we have.

$$\sigma_1 = 2\sqrt{M_t \sigma_0} - \sigma_2 \tag{4.25}$$

For the total mass of the worktable of $24.418\ kg$ and identified viscous friction in the previous step we get $\sigma_1 = 361.49\ Ns/mm$.

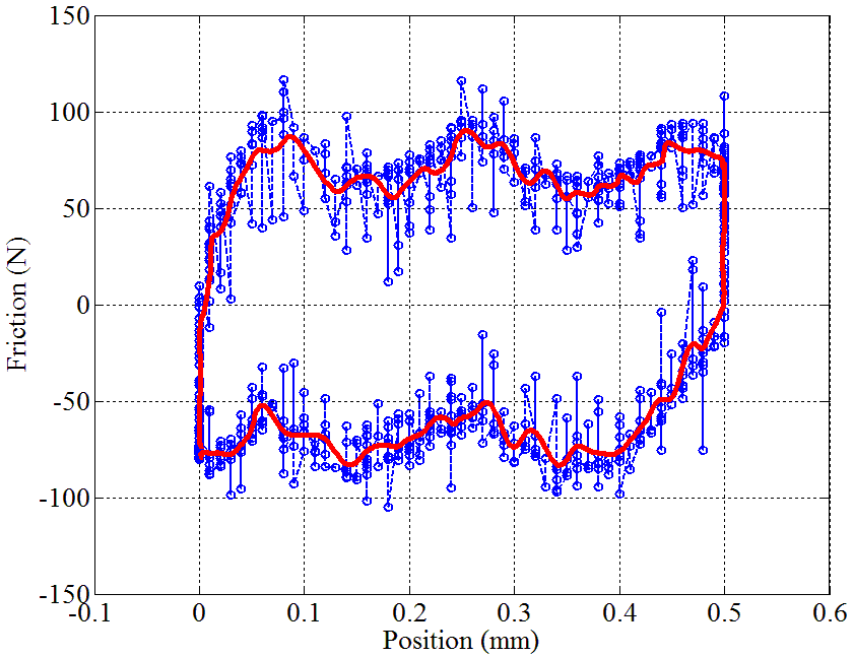

Figure 4.11. *The hysteresis between friction force and displacement in presliding region*

As it can be seen from the hysteresis there is an oscillatory pattern which is symmetric. This can be investigated by the stick-slip behavior where the worktable sticks until the friction force equals to breakaway force and it starts to slide and friction force decreases. The number of steps can significantly affect the hysteresis pattern so that the larger the stick slip the larger will be the oscillations in the slider [36]. Figure 4.12 shows the determination of the stiffness factor in presliding region.

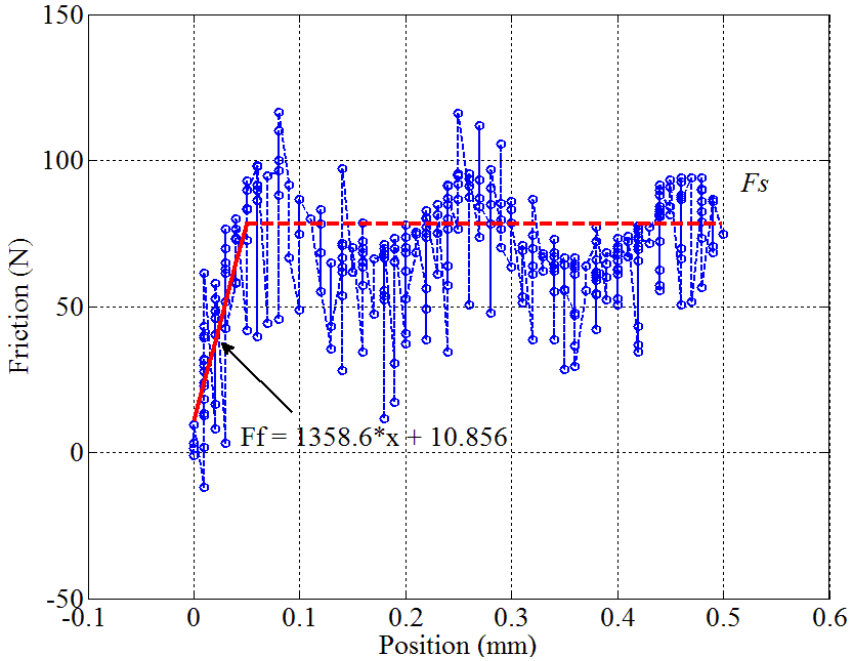

Figure 4.12*Stiffness and microdamping determination*

4.5 Indirect grinding force measurement from the infeed axis motor torque

Indirect cutting force measurement has been focus of many studies recently in order to achieve autonomous machine tools that can control the cutting conditions and failure detections [37, 38, 39, 40, and 41]. Although many studies have been carried out for milling, turning, and drilling processes, very few research works evaluated the feasibility of indirect grinding force measurement by the feed motor torque. Grinding force can be considered as one of the condition monitoring tools that provides valuable information about the grinding process to prevent high forces which cause grinding wheel wear. Measurement of the grinding force typically is carried out using dynamometers that are expensive. A dynamometer can cost over $20000. This type of measurement is also suffers from the mounting issues which differ from one machine to another. This mounting greatly influences the overall stiffness of the machine tool. Indirect grinding force measurement by monitoring the thrust force of the infeed axis is presented here. In this case the estimation of the grinding force is performed only by means of an inexpensive current sensor in the motor without implementation of any additional sensors.

Friction, inertia, and the grinding forces are the total external forces that affect the thrust force of the servo drive in the infeed axis. This can be stated as

$$F_t = k_f I = F_{grinding} + F_f + M_t \frac{dv}{dt} \tag{4.26}$$

A dual mode grinding cycle of grinding process is depicted in the Figure 4.13. The infeed motion of the grinding wheel is carried out up to achieve a certain depth of cut in roughing. The spark out comes after the infeed motion step. This step is carried out when the grinding wheel axis is stopped and the velocity of the axis becomes zero, but the actual infeed velocity due to the deflection in the grinding system is not zero. At last the grinding wheel is retracted. In this case the grinding wheel does not have any contact with the workpiece. The velocity of the infeed in spark out stage is analogous to a stationary axis in 2D milling process as it is depicted in the Figure 4.14. The stationary axis is controlled so that it does not move. The current in this state has various patterns and behaviors which are characterized by the cutting force, and stick-slip friction behavior of the axis [42, 43, 44].

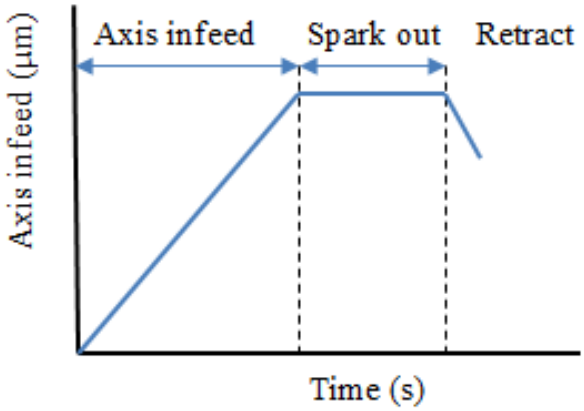

Figure 4.13 *A dual mode grinding cycle*

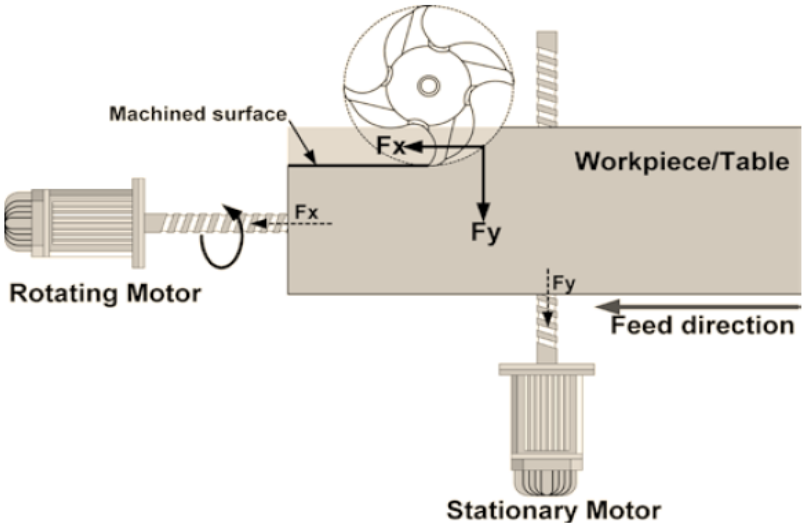

Figure 4.14 *Schematic the rotating and stationary axis in a 2D milling process [45]*

A grinding measurement is planned to evaluate the feasibility of friction estimation based on the infeed axis of the test rig. The rotational speed of the workpiece and the grinding wheel for this measurement are 133 rpm, and 1680 rpm. The initial diameter of the workpiece for this measurement is 110 mm and the grinding wheel outer diameter is 200 mm. The infeed and infeed rate of the axis for this measurement are 80 µm , and 0.02 mm/s. The measurements are carried out without use of coolant. There is the following relationship between the infeed rate and the depth of cut based on the workpiece rotational speed

$$a = \frac{v_f}{\omega_w} \tag{4.27}$$

The grinding force signal as the most important component in the thrust force Fourier transformation can be found. The frequency of the main component is located at f_F where

$$f_F = \frac{\omega_g}{2\pi} = 28\,Hz \tag{4.28}$$

In the above equation the rotational speed of the spindle ω_g is in rad/sec.

The effects of ball screw over the thrust force signal are nonlinear and they are reflected in the signal as harmonics and sub-harmonics centered at $f_B$which is determined as below

$$f_B = \frac{v_f \cdot p'}{2\pi} \tag{4.29}$$

Where p' is the pitch of the ball screw in rev/mm. This frequency for 0.02 mm/sec infeed velocity becomes $3.18\times10^{-4}Hz$.

Figures 4.15, 4.16, and 4.17 show the Fourier transform of the thrust force signal. Figure 4.15 depicts the increase in the amplitude of the thrust force signal in infeed grinding compared to the air grinding and spark out states. The signal implies not only the information about the grinding conditions but also contains undesired components in the form of high-frequency noise, and the ball screw effects.

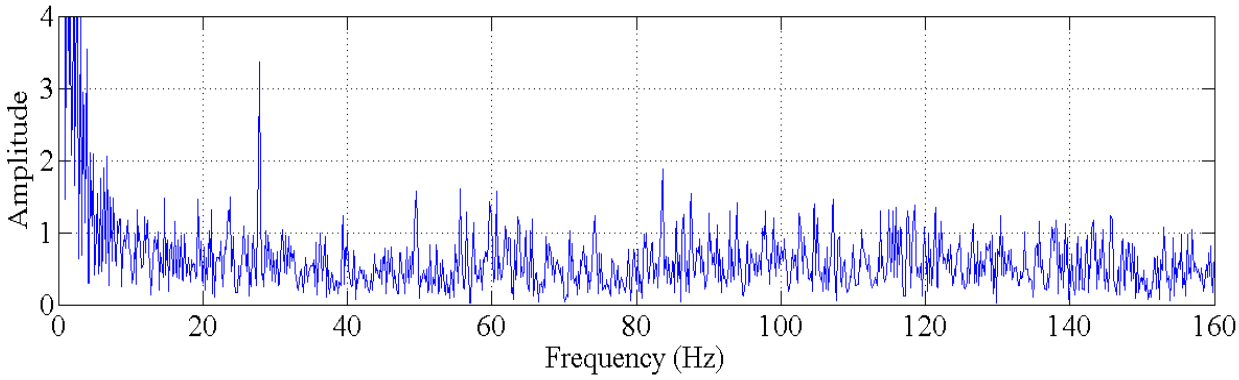

Figure 4.15 *Fourier transform of the thrust force in infeed grinding*

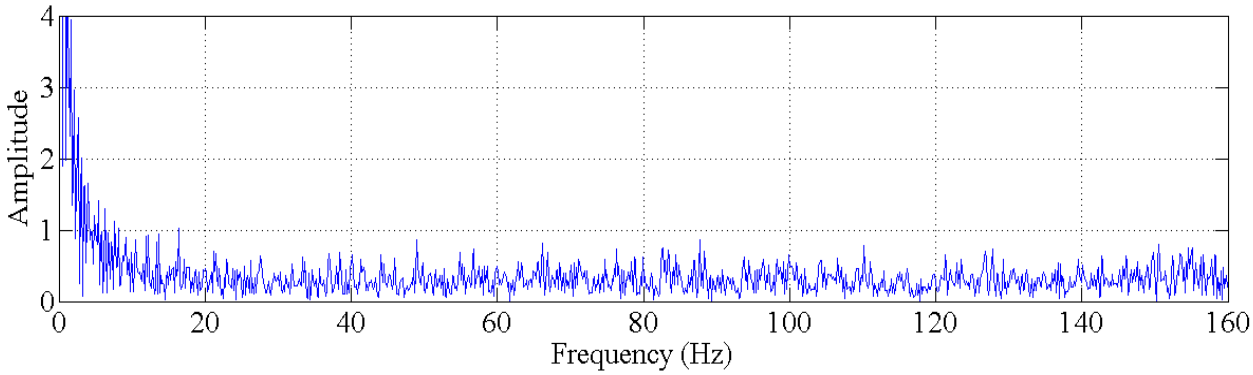

Figure 4.16 *Fourier transform of the thrust force in spark out stage*

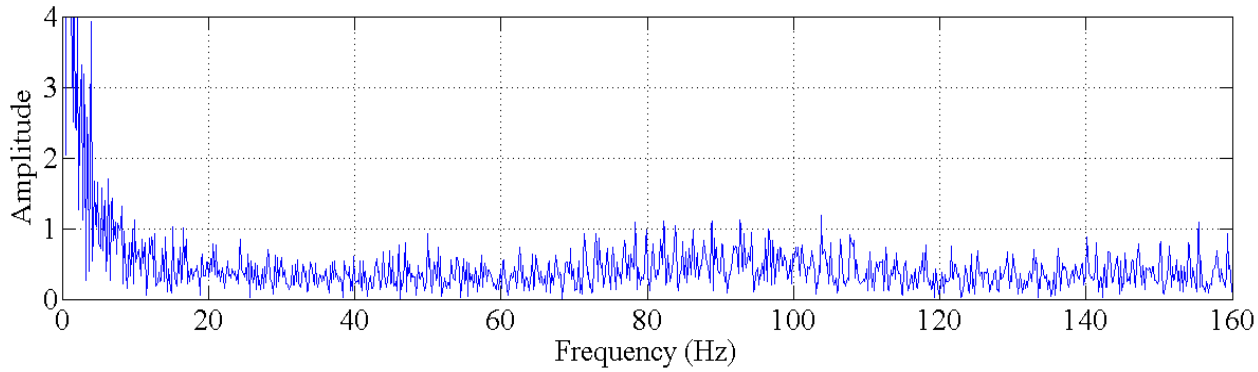

Figure 4.17 *Fourier transform of the thrust force in air grinding*

Figure 4.18 and 4.19 illustrate the zoomed view of the Fourier transform for infeed and spark out stages. As it can be observed from the Figure 4.18 the three lowest harmonic components of the grinding spindle is detected for the infeed case; however the identification of the harmonic componenets from the spark out stage is not possible and the signal has considerably lower amplitude in comparison with the infeed stage as it was expected.

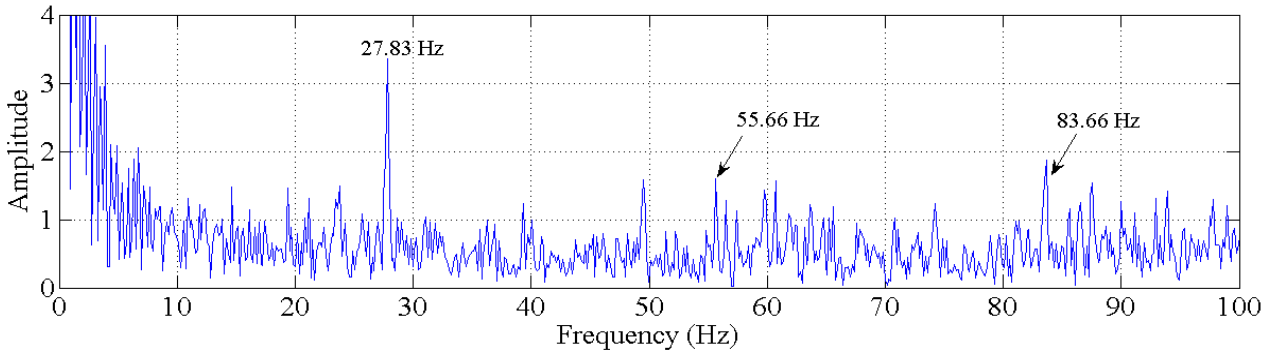

Figure 4.18 *Zoomed view of Fourier transform of the thrust force in grinding*

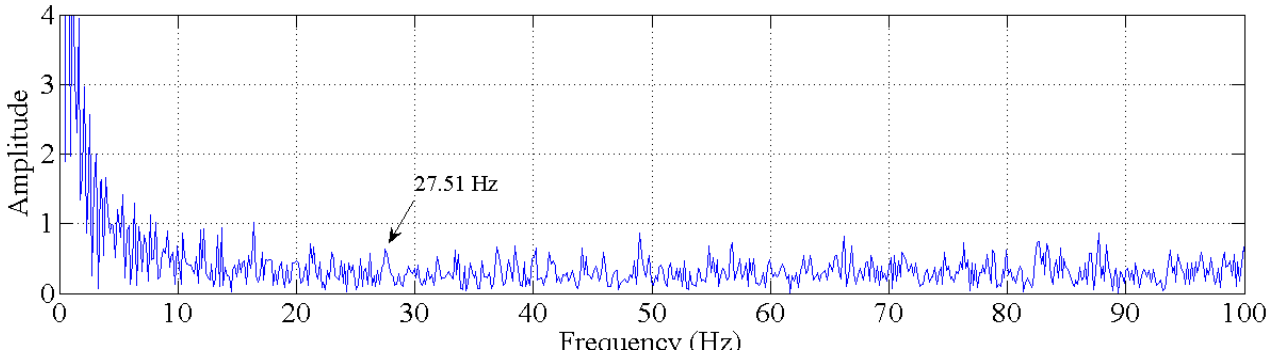

Figure 4.19 *Zoomed view of Fourier transform of the thrust force in spark out*

The thrust force of the infeed axis for three cases has been shown in the figures below. Figure 4.20, 4.21, and 4.22 are the demonstration of the thrust force for air grinding, infeed grinding and the spark out conditions.

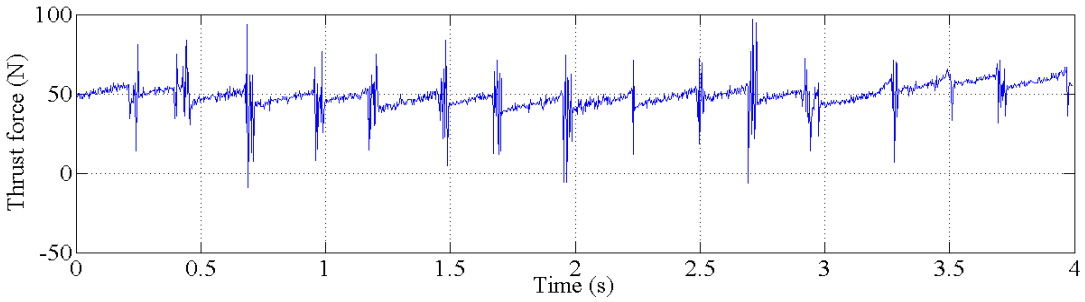

Figure 4.20*Thrust force of the infeed drive in air grinding*

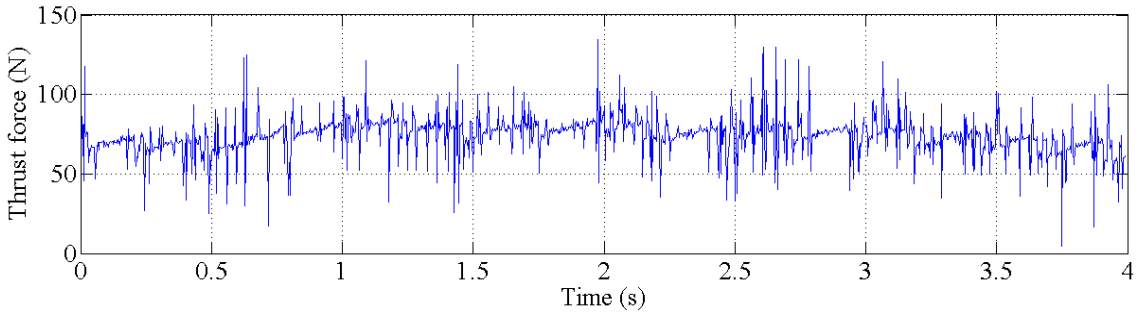

Figure 4.21 *Thrust force of the infeed drive in grinding*

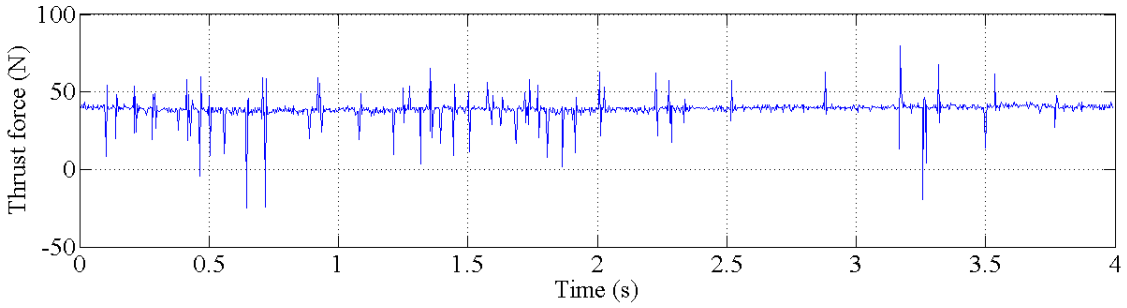

Figure 4.22 *Thrust force of the infeed drive in spark out*

As it can be seen from the Figure 4.22 the thrust force signal in spark out stage of the grinding shows some intermittent bounces and this pattern is decayed at the end of the period. This dynamic behavior of the signal when the feed rate is remained ideally zero can be explained by the grinding force during the spark out stage as it drops over the period. In practice due to the infinitesimal rotation of the rotor at this point we can conclude that the bounces in the thrust force of the motor is related to the grinding force. In this stage the disturbances affecting the thrust force of the infeed axis consists of grinding force, and stick-slip friction. The stick–slip friction represents the resistance to relative motion between contact planes; it decreases suddenly when the stick–slip state collapses due to a thrust force over a given magnitude. Because the current of the stationary feed motor reflects both the grinding force and the stick– slip friction, the grinding force can be estimated if the stick–slip friction is assumed to have a constant influence. In this state, the friction force cannot be constant because the infeed velocity of the slide is zero. With this in mind, the friction force is balanced with the grinding force in case of the grinding force is smaller than the friction force, and the axis is moved by the grinding force in case this force is larger than the friction force in the slide. The friction force in the spark out stage has larger amplitude than in infeed motion [46].

Due to the low resolution of the available encoder and inconsistency of the stick-slip friction in spark out the friction force cannot be determined by means of velocity estimation signal.

Figure 4.23 shows the local thrust force and the grinding force estimation signal which is the subtraction of the steady-state friction value at 0.02 mm/s from the total thrust force. The friction value based on the identification done for the axis is 64.5 N, and the resulting grinding force is 9.59 N.

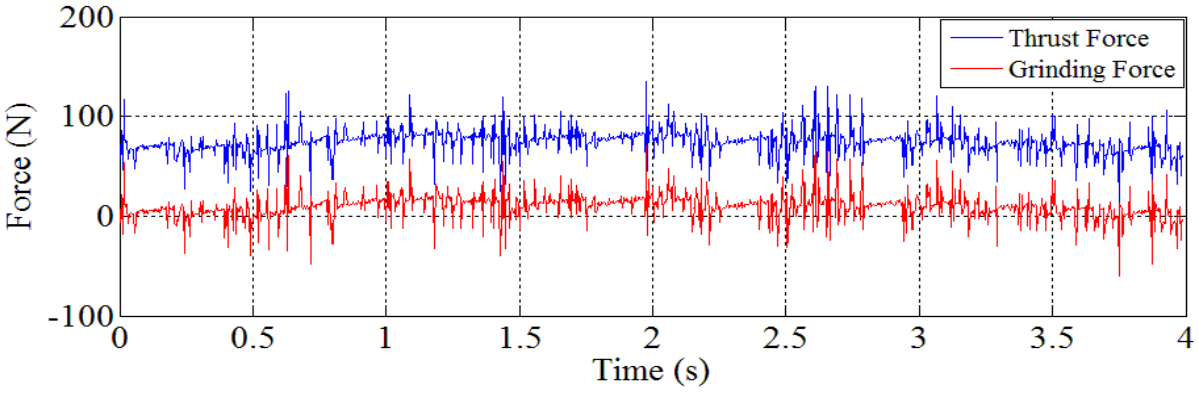

Figure 4.23 *Comparison of the grinding and thrust force*

5. TRANSVERSE AXIS

Transverse axis of the cylindrical grinder is used for the traverse grinding cut. Traverse grinding cut is mainly used to make cylindrical parts with good surface quality. This process is much more complex in comparison with plunge grinding where only the infeed axis is used to achieve certain amount of penetration into the workpiece. The grinding process in traverse cut tends to be unstable under condition of lower tranverse speeds of the workpiece. This was shown in the section 3.2 where higher overlap ratios resulted worse stability boundaries. In order to be able to carry out the traverse grinding cut with the experimental machine, the movement of the workpiece along the grinding wheel is performed using a ball screw drive. The cross feed of the workpiece generates two chamfer with a sharp preliminary edge followed by a smoother edge. When the transverse direction is reversed at the end of the workpiece, the same process repeats on the other edge of the grinding wheel. The precision of this axis directly affects the overlap ratio for the traverse grinding cut of the workpieces.

5.1 Calculation of the ball screw drive parameters

In this section the calculation of the driving torque for the ball screw in transverse axis is explained.

The total mass of the transverse table with the maximum dimension of the workpiece and all the masses which are present on this table is $m_{table} = 35\,kg$. The inertia of this mass is determined by considering the conversion factor between rotational and translational movement as given below.

$$J_{table} = m_{table}(\frac{p_t}{2\pi})^2 \approx 1.42\times10^{-5}\,kgm^2 \tag{5.1}$$

In the above equation parameter p_t denotes the pitch of the ball screw in the transverse axis of the machine.

The inertia of the ball screw based on the dimension of the ball screw is determined as below

$$J_B = \frac{\pi}{32}\rho_B l_B d_B^4 \approx 2.13\times10^{-6}\ kgm^2 \tag{5.2}$$

The ball screw pitch is $4\,mm$ and the length and the diameter of the ball screw are $670\,mm$, and $8mm$ respectively.

The total load inertia of the axis is determined as

$$J_{total} = J_{table} + J_B \approx 1.633 \times 10^{-5}\ kgm^2 \tag{5.3}$$

The fixed-fixed mounting setup (two support bearings at the ends) provides high stiffness for the feed drive. In order to take the resonance factor into consideration the permissible speed is determined to prevent the approach of ball screw speed to the natural frequency.

$$n_c \approx \frac{60\lambda^2}{2\pi l_B^2}\sqrt{\frac{E_B I_B}{\rho_B A_B}} = 3467\,rpm \tag{5.4}$$

l_B is the distance between mounting positions, E_B is the elastic modulus, I_B is the second moment of inertia, and λ is the support factor. The support factor for the fiexed – fixed boundary conditions is assumed to be 4.

The operating rotational speed of the transverse axis for a maximum table speed of $0.05\ m/s$ and the ball screw pitch is calculated as

$$N_m = \frac{60 \cdot v_g}{p_t} \approx 750\,rpm \tag{5.5}$$

The $F_{Load}$is the load force of the transverse axis and is obtained from the following equation

$$F_{Load} = F_{cut} + F_{friction} \tag{5.6}$$

Since there is not any cutting force affecting this direction the thrust force becomes as follows

$$F_{Load} = \mu_L m_{table} g \approx 34.335\ N \tag{5.7}$$

$$T_{Load} = \frac{F_{Load} p_t}{2\pi} + \frac{\mu_0 F_0 p_t}{2\pi} \approx 0.024\ Nm \tag{5.8}$$

In the above equations $\mu_L$and μ_0 are frictional coefficient of the sliding surface and the preload nut respectively. Here the ball screw preload is $F_0 = \frac{1}{3} F_{Load}$.

By taking the safety factor into account $S_f = 1.5$ the load torque is recalculated as $0.036\ N.m$. Based on the calculation for the drive an AKM21F-ANMN2-00 brushless servo motor is chosen with rated speed of $1300\,rpm$ and the rated torque of $0.345\ N.m$. In order to determine the inertia torque with consideration of the rotor inertia value as $J_{rotor} = 0.107\ kg.cm^2$and an acceleration/deceleration time of $t_1 = 0.1\ s$ we have

$$T_I = \frac{\left(J_{total} + J_{rotor}\right) \cdot N_m}{9.55 \cdot t_1} \approx 0.021\,Nm \tag{5.9}$$

Figure 5.1 shows the servo motor NI 9502, and NI 9411 modules. The encoder signal is read using NI 9411 and NI 9502 module provides output for the brushless servo motor.

Figure 5.1 *AKM21F-ANMN2-00 brushless servo motor, NI 9502, and NI 9411 modules [47]*

5.2 Field Oriented and Trapezoidal commutation on NI 9502

Nowadays most of the advanced servo systems employ an inner control loop that regulates the torque of the motor. The torque of the brushed type motors are easily controlled since the motor uses the commutation. The brushed type servo motors do not have the self-commutating capability and therefore have more complicated control. In this case the motor current and voltage are controlled separately as a function of position of the rotor.

5.2.1 Trapezoidal commutation

Trapezoidal commutation uses the three Hall Effect sensors embedded in the motor to create the digital signals which measures the rotor position within 60 degree sectors. At any time current through two of the three phases of the motor is sent, and the phase transition is carried out by means of Hall Effect sensor state changes. This type of commutation is simple for implementation however it can create torque ripple at low speeds. This type of commutation is well suited for the application where a coarse motion of the rotor is not problematic. This fact makes this type of commutation undesirable for the traverse movement of the workpiece as a smooth motion of the roll in the traverse movement is desired.

5.2.2 Field Oriented Commutation (FOC)

Field oriented control commutation allows smooth motion at low speeds. This type of commutation is created to solve the problem of current change nature by controlling the current space vector directly in the d-q reference frame of the rotor. In the ideal case, the current space vector is fixed in magnitude and direction (quadrature) with respect to the rotor, irrespective of rotation. This means the Field-oriented control allows the controller to operate unaffectedly from sinusoidal motor current and voltage changes, for low speeds. Similarly, the voltages to be applied to the motor are mathematically transformed from the d-q frame of the rotor to the three phase reference frame of the stator before they can be used for PWM output.

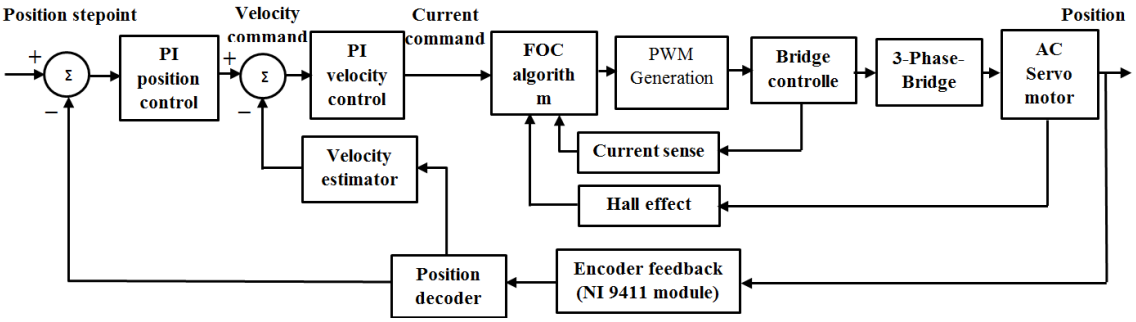

Figure 5.2 *The control block diagram by NI 9502 FOC commutation [48]*

In this technique two PI controllers are used; one for the direct current component, and one for quadrature current. The input to the controller for the direct current and has zero input. This drives the direct current component to zero and therefore forces the current space vector to be exclusively in the quadrature direction. Since only the quadrature current produces useful torque, this maximizes the torque efficiency of the system. The second PI controller operates on quadrature current and takes the requested torque as input. This causes the quadrature current to track the requested torque, as desired.

The control block diagram of the transverse axis by FOC commutation is illustrated in the Figure 5.2. As it can be observed the control scheme consists of Proportional Integral (PI) control loop for position, velocity and an inner current loop. The tuning of the gains for this axis is done using Ziegler-Nichols method. The ball screw drive in transverse axis of the machine, with support bearing and guideways has been demonstrated in the figure 5.3.

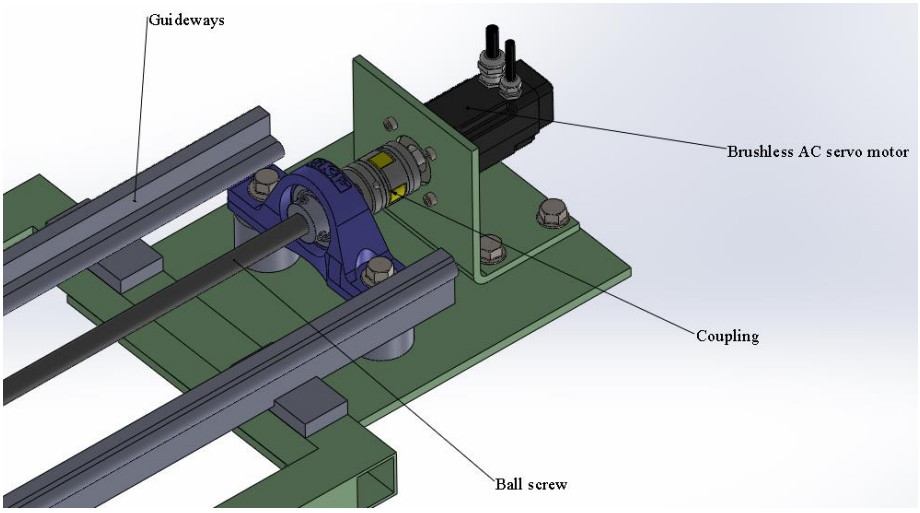

Figure 5.3*The ball screw drive layout in the transverse axis*

6. WORKPIECE ROTATIONAL AXIS

As mentioned earlier in cylindrical grinding of rolls the peripheral speeds of the workpiece is considerably lower than the grinding wheel. In the case of workpiece with peripheral speeds of lower than $40\ \mathrm{m/min}$, the use of a gearhead is advantageous. Application of the motor with integrated spur gearhead reduces the system size noticeably. The servo application of motor with gearhead can bring about high resolution of the speed control since the speeds are reduced by transmission ratio. The inertial matching in these motors has a great significance since servo motors are normally generating more torque relative to frame size that results in greater inertial mismatches between the motor and the load.

Based on the workpiece maximum dimension and the inertia load for the workpiece a permanent magnet DC motor with spur gearhead is chosen for the test rig. The BCI6355 DC motor has a gear reduction ratio of $27.6:1$ in two stages with an output power and torque of $75\ watts$, $6\ N.m$ respectively. A G05 incremental optical encoder with 100 pulses per revolution is attached to the DC motor for reading the rotational angle of the rotor.

The control scheme used for controlling of this axis is based on a PI velocity and a PI inner loop current control in LabVIEW FPGA environment. Ziegler-Nichols tuning method is used for tuning of the control gains. In the first step control parameters of the current loop is tuned and then the velocity loop gains are chosen based on the current loop values selected in the previous step. The current and velocity loop rates for the controller are $50\mu s$, and $250\ \mu s$ respectively. Figure 6.1 shows the control block diagram implementation for the DC motor by means of NI9505 servo drive. The velocity loop output commands are the current commands which are sent to the current loop and this signal in the current loop creates a Pulse Width Modulation (PWM) signal which is sent to the motor to generate the desired torque of the motor. The rotational velocity of the motor is estimated by the second derivative term of the encoder value.

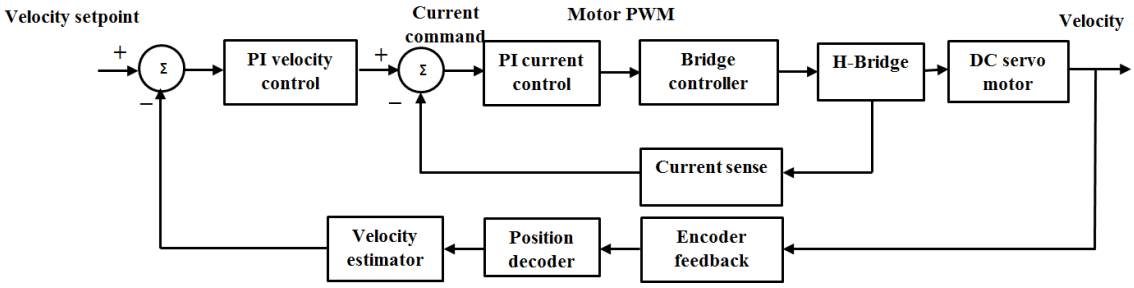

Figure 6.1 *The control block diagram of the DC motor with spur gearhead by NI 9505[49]*

Figure 6.2 is the illustration of the DC motor with spur gearhead and NI 9505 servo drive for the rotational movement of the workpiece.

Figure 6.2 *BCI6355 Permanent magnet DC motor with spur gearhead with G05 Optical incremental encoder [50], and NI 9505 Full H-Bridge Brushed DC Servo Drive Module [47]*

The rotational axis of the machine with motor and and spur gearhead attached to the workpiece with a coupling is shown in Figure 6.3. As it can be seen the workpiece has been assembled with bolted flanges for the connection in the ends.

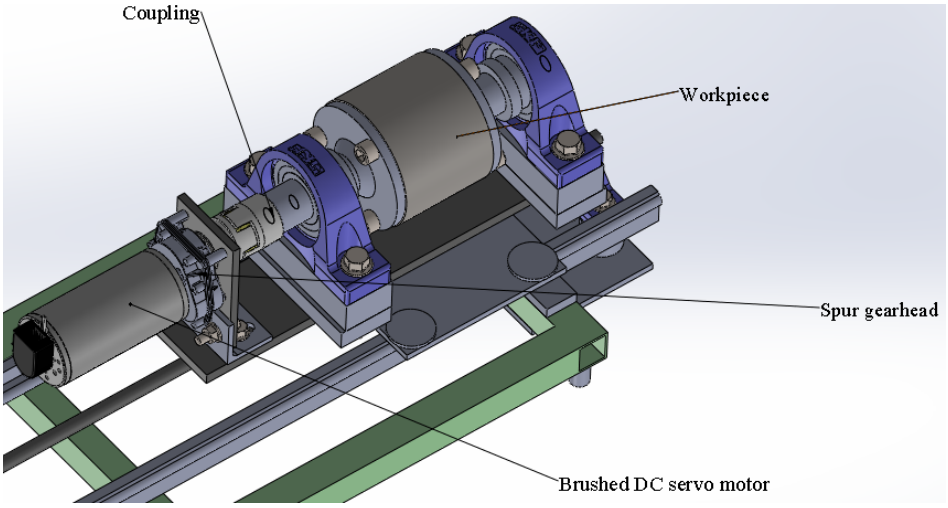

Figure 6.3*Rotational axis of the machine*

For the motion control of the axes in the machine a CompactRIO 9024 Real-Time (RT) embedded controller and a NI 9118 chassis with eight slots are used. Figure 6.4 shows the motion control system with the DC power supplies providing the enough power for the controller and the motion control modules. This controller is capable of up to 40 MHz control loop rates with Field Programmable Gate Array (FPGA) based backplane.

The computer software and hardware used to run the servo axes of the machine are based on the National Instruments LabVIEW and CompactRIO real time embedded controller. LabVIEW provides interface through which programs for the RIO can be

written and compiled in order to drive the axes. Figure 6.3 shows the CompactRIO controller and the modules used for the servo control of the axis in the test rig.

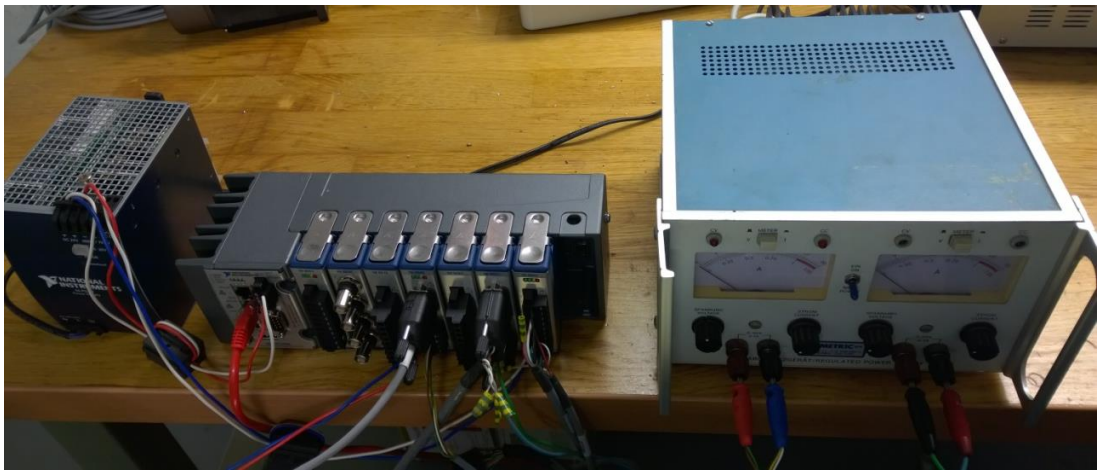

Figure 6.4 *CompactRIO, motion control modules, and DC power supplies*

7. CONCLUSION

In this master's thesis, design and implementation of an experimental cylindrical grinding machine for plunge and traverse grinding cut is developed. The cylindrical grinder in this study is capable of grinding of the workpieces with maximum $150\ mm$ diameter and $200\ mm$ length. The workpiece rotational speeds can reach speeds as high as $150\ rpm$ by means of a spur gearhead attached to a permanent magnet DC motor in this axis to reduce the speeds by a ratio of 27.6. The grinding spindle is capable of maximum rotational speeds up to 1690 rpm using a belt transmission element. The grinding process used in the experimental setup uses a dual mode grinding cycle with infeed motion of the grinding axis for rough grinding of the workpieces, which is followed by a sparkout stage. The servo control of the transverse axis ensures a constant overlap ratio for the whole length of the workpiece.

Due to the significance of the chatter vibration in cylindrical grinding process a traverse grinding case is presented. In order to estimate the boundary layers for a chatter free cutting condition in a traverse grinding cut a discrete model for the interaction between the workpiece and the grinding wheel is developed with two time delays. Since both of the grinding wheel and the workpiece have rotational movement two cases for the stability analysis has been implemented. In the first case the grinding wheel rotational velocity is changed over a range and the workpiece rotational speed is kept constant for the period. In the second case the inverse action is considered. Based on the stability boundaries identified in the previous step the time domain grinding forces for the normal and tangential axis as well as the displacement of the grinding wheel and the workpiece are presented.

In order to estimate the grinding force during a dual mode grinding cycle a new method based on the thrust force monitoring for the infeed axis of the grinding machine is proposed. The friction, inertia, and the grinding forces as disturbances on the thrust force are considered. The inertial force of the motion is calculated based on the known inertia value for the drive and the acceleration estimation from the second derivative of the encoder angular displacement values. The nonlinear friction effect as one of the major disturbances affecting the servo drives have been identified in this case for the infeed motion of the slide way for the air grinding condition. LuGre model as one of the powerful models which captures most of the friction characteristics has been used and the static and the dynamic parameters are determined. The static parameters of the model are derived using the Stribeck curve of the drive. In order to demonstrate the dynamics properties of the infeed axis a short stroke reciprocating motion is used. In this case the presliding behavior of the drive is shown and the microdamping and stiffness parame-

ters for this region are determined from the hysteresis curve. The infeed motion of the grinding is carried out at a constant feed rate. The grinding force associated with the infeed motion of the grinding wheel can be estimated by subtraction of the total thrust force and the friction force identified for that specific feed rate. The frequency content of the signal for infeed, spark out and the air grinding cases have been compared to depict the harmonics related to the grinding force. Detection of the grinding harmonics in the Fourier transformation in the case of grinding is more difficult in comparison with the milling or turning process. However the three components of the grinding harmonics are identified for the infeed motion. The harmonics detection is not possible in the case of spark out stage due to the inconsistency of the bounces which are the result of change in the angular displacement of the feed drive caused by the grinding force at this stage.

Further investigations needs to be conducted on the test rig for finding the relationship between the grinding force and the nonlinear friction effect in the slide way. The friction effect can play an important role in the case of spark out stage since there is not any control input from the motor. In this situation the friction and grinding force are balanced with each other as the outcome of the stick-slip phenomenon. This means the final product surface quality is highly affected by this phenomenon.

REFERENCES

[1] S. Kalpakjian, Manufacturing Engineering and Technology, Upper Saddle River, NJ, Prentice Hall, 2001.

[2] V. Singh, P. V. Rao, S. Gosh, Development of specific grinding energy model, International Journal of Machine Tools & Manufacture, vol. 60, 2012, pp. 1242-1253.

[3] W. B. Rowe, Principles of Modern Grinding Technology (Second Edition), William Andrew Applied Science Publishers, 2014, pp. 335-348.

[4] I.D. Marinescu, M. Hitchiner, E. Uhlmann, W.B.Rowe, I. Inasaki, Handbook of Machining with Grinding Wheels, (Hard Cover), 2007.

[5] N. L. d. Lacalle, A. L. Lamikiz, Machine Tools for High Performance Machining, Springer-Verlog London Limited, 2009.

[6] E. Smejkal, H. Lutze, W. Degner, Spanende Formung. Theorie, Berechgnung, Verlag Technik, Berlin 2009.

[7] R. G. Budynas, J. K. Nisbett, J. E. Shigley, Shigley's Mechanical Engineering Design, Eighth Edition, New York, McGraw-Hill, 2011, pp.862.

[8] S. M. Kim, J. H. Ha, S. H. Jeong, S. K. Lee, Effect of joint conditions on the dynamic behaviour of a grinding wheel spindle, International Journal of Machine Tools & Manufacture, vol.41 2001, pp.1749-1761.

[9] Y. Altintas, and C. Yuzhong, Modelling of spindle-bearing and machine tool systems for virtual simulation of milling operations, international journal of machine tools and manufacture, vol.47, no.9, 2006, pp.1342–1350.

[10] T. Insperger, Stability analysis of periodic delay-differential equations modelling machine tool chatter, A Dissertation Submitted in Partial Fulfillment of the Requirements for Degree of Doctor of Philosophy in Department of Applied Mechanics, Budapest University of Technology and Economics, 2002.

[11] S. J. Zhang, and S. To, A theoretical and experimental study of surface generation under spindle vibration in ultr precision raster, International Journal of Machine Tools and Manufacture, vol.75, 2013, pp.36–45.

[12] K. J. Kalinski, and M. A. Galewski, Chatter vibration surveillance by the optimal-linear spindle speed control, Journal of Mechanical Systems and Signal Processing, vol.25, 2011, pp.383–399.

[13] I. Mañé, V. Gagnol, B.C. Bouzgarrou, and P. Ray, Stability-based spindle speed control during flexible workpiece high-speed milling, International Journal of Machine Tools & Manufacture, 2008, no.2, vol.48.

[14] L. Yuan, V. M. Järvenpää, E. Keskinen, , and M. Cotsaftis, Simulation of roll grinding system dynamics with rotor equations and speed control, Journal of Communication in Nonlinear Science and Numerical Simulation, 7, 2002, pp.95–116.

[15] V. M. Järvenpää, L. Yuan, H. K. Shirvani, and F. Mehmood, Modelling of tangential vibrations in cylindrical grinding contact with regenerative chatter, Proceedings of the 7th International Surveillance Conference, the Institute of Technology of Chartres, France, Oct 2013, pp.29-30.

[16] Y. Yan, J. Xu, and M. Wiercigroch, Chatter in a traverse grinding process, Journal of Sound and Vibration, vol. 333, 2014, pp.937-953.

[17] P. Kim, J. jung, S. Lee, and J. Seok, Stability and bifurcation analyses of chatter vibrations in a nonlinear cylindrical traverse grinding process, Journal of Sound and Vibration, vol.332, 2013, pp.3879-3896.

[18] K. W. Chung, Z. Liu, Nonlinear analysis of chatter vibration in a cylindrical transverse grinding process with two time delays using a nonlinear time transformation method, Journal of Nonlinear Dynamics, vol.66, 2011, pp.441456.

[19] V. M. Järvenpää, L. Yuan, H. K. Shirvani, On vibroacoustic analysis of grinding contact vibrations, Proceedings of the 21st International Congress on Sound and Vibration, 13-17 July 2014.

[20] L. Yuan, V. M. Järvenpää, S. Virtanen, Hopf bifurication of nonlinear contact force in grinding system, Proceedings of 21st International Congress on Sound and Vibration, 13-17 July 2014.

[21] L. Yuan, , E. Keskinen, , and V. M. Järvenpää, Stability analysis of roll grinding system with double time delay effects, UTAM Symposium on Vibration Control of Nonlinear Mechanisms and Structures Solid Mechanics and its Applications, no.130, 2005, pp.375–387.

[22] Zh. Liu, and G. Payre, Stability of doubly regenerative cylindrical grinding process, Journal of Sound and Vibration, vol.310, Issue.(3–5), 2007, pp.950–962.

[23] H. K. Shirvani, L. Yuan, V. M. Järvenpää, The influence of chatter vibration on the cylindrical transverse grinding machine spindle, Proceedings of the 21st International Congress on Sound and Vibration, 13-17 July 2014.

[24] V. Jouppila, A. Gadsden, G. Bone, A. Ellman, S. Habibi, Sliding mode control of a pneumatic muscle actuator system with a PWM strategy, International Journal of Fluid Power, vol. 15, Issue 1, 2014, pp.19-31.

[25] V. Jouppila, A. Gadsden, A. Ellman, Modeling and identification of a pneumatic muscle actuator system controlled by an On/Off solenoid valve, Proceedigns of 7th Fluid Power Conference Aachen, 22-24.5.2010, pp 167-182.

[26] Festo product data sheets. Available at: http://www.festo.com.

[27] SKS product data sheets. Available at: http://www.sks.fi/www/_products

[28] N. L. Bernstein, Force Sensor Modeling and Friction Compensation for Haptic Interfaces, adissertation submitted in partial fullfilment of the requirements for degree of Doctor of Philosophy in College of Engineering and Applied Scieneces Department of Aerospace Engineering Sciences, 2007.

[29] P. Dahl, A solid friction model, The Aerospace Corp., El Segundo, CA, Tech. Rep. TOR-0158(3107–18) –1, 1968.

[30] C. Canudas, H. Olsson, K. J. Åström, P. Lischinsky, A new model for control of systems with friction, IEEE Transactions on Automatic Control, vol. 40, no. 3, Mar 1995, pp. 419–425.

[31] K. J. Åström, C. Canudas, Revisiting LuGre friction model, IEEE control Systems, vol.28, Issue.6, Dec 2008, pp.101-114.

[32] H. K. Shirvani, V. M. Järvenpää, L. Yuan, Dynamic modelling and control of an experimental cylindrical grinder in presence of nonlinear friction effect, Proceedings in Research Conference in Technical Disciplines, RCITD 2013, 18-22 November 2013, Slovak Republic.

[33] R. H. A. Hensen, M. J. G. van de Molengraft, M. Steinbuch, Frequency Domain Identification of Dynamic Friction Model Parameters, IEEE Transactions on Control Systems Technology, vol. 10, no. 2, Mar 2002, pp. 191–196.

[34] F. Vargas, R. Edson, Identification and Friction Compensation for an Industrial Robot Using Two Degrees of Freedom Controllers. Control Automation Robotics and Vision Conference, vol. 2, Dec 2004, pp.1146–1151.

[35] MathWorks, MATLAB Signal Processing Toolbox. User's manual, 2014.

[36] A. Kanai, M. Miyasita, H. Nishihara, and J. Yoshioka, A Study of Frictional Characteristics of Slide-way in Microdynamics, Proceedings of the ASPE Annual Conference, 1992, pp. 126-129.

[37] R. Sato, M. Hasegawa, K. Shirase, Cutting force monitoring based on the frequency analysis of feed motor torques, Journal of SME Japan, vol.2, 2013, pp.7-12.

[38] R. R. Jesús, H. Gilberto, T. Iván, J. J. Carlos, Driver current analysis for sensorless tool breakage monitoring of CNC milling machines, International Journal of Machine Tools and Manufacture, vol.43, Issue.15, 2003, pp1529-1534.

[39] H. Liu, L. Lian, B. Li, X. Mao, S. Yuan, and F. Peng, An approach based on singular spectrum analysis and the Mahalanobis distance for tool breakage detection, Journal of Mechanical Engineering Science, 2014, pp.1-12.

[40] B. Denkena, H. K. Tönshoff, X. Li, C. Lapp and J. Imiela, C. Lapp, Analysis and control/monitoring of the direct linear drive in end milling, International Journal of Production Research, vol.42, no.24, 2004, pp.5149-5166.

[41] Y. H. Jeong, D. W. Cho, Estimating cutting force from rotating and stationary currents on a milling machine, International Journal of Machine Tools & Manufacture, vol.42, 2002, pp.1559-1566.

[42] D. Kanopp, Computer simulation of stick-slip friction in mechanical dynamic systems, Journal of Dynamic Systems Measurement and Control, vol.107, 1985, pp.100-103.

[43] K.C. Cheok, H. Hu, N.K. Loh, Modeling and identification of a class of servomechanism systems with stick-slip friction, Journal of Dynamic Systems Measurement and Control, vol.110, 1988, pp.324-328.

[44] L. F. Gasca, G. H. Ruiz, R. P. Vera, R. J. R. Troncoso, W. L. Tafolla, Sensorless tool failure monitoring system for drilling machines, International Journal of Machine Tools and Manufacture, vol.46, Issue 3-4, 2006, pp.381-386.

[45] Y. H. Jeong, D. W., Cho, An investigation of the characteristics of the stationary feed motor current in NC machines, International Journal of Manufacturing Technology, vol.22, 2003, pp.553-561.

[46] H. K. Shirvani, L. Yuan, V. M. Järvenpää, Investigation of cylindrical grinding force with consideration of friction in feed drive, Proceedings of 8th European Nonlinear Dynamics Conference, ENOC 2014, July 6-11 2014, Vienna, Austria.

[47] National Instruments products. Available at: http://www.ni.com/products/

[48] NI 9502 Brushless Servo Motor Drive
http://www.ni.com/pdf/manuals/375480a.pdf

[49] NI 9505 Brushed Servo Drive
http://www.ni.com/pdf/manuals/374211f.pdf

[50] Zeitlauf products. Available at:
http://www.zeitlauf.com/product_info/product_range.html

8. APPENDICES

Appendix 1: CAD model of the test rig

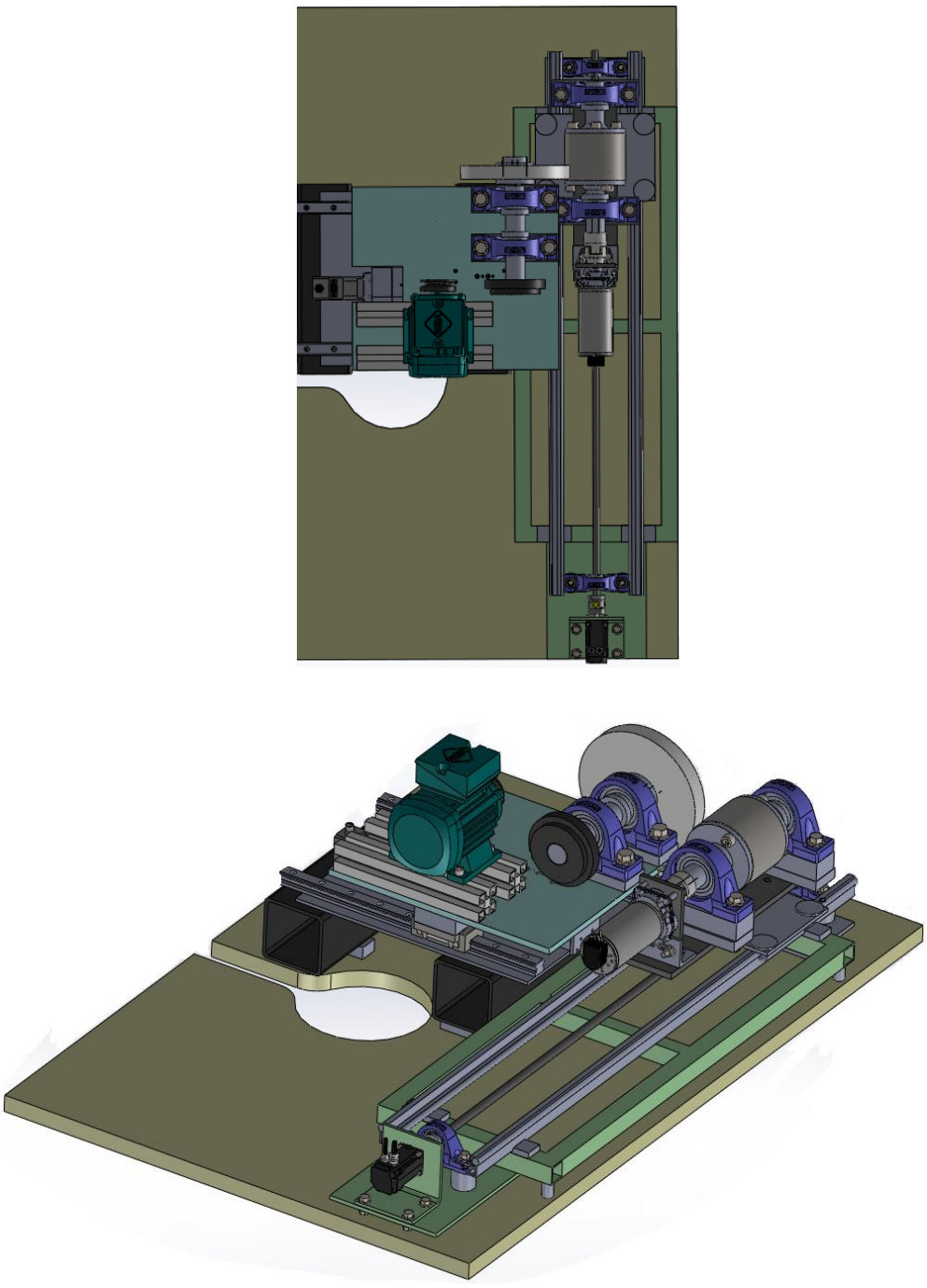

Figure 8.1 *CAD model of the test rig*

Appendix 2: Test rig in two different prospective

Figure 8.2 *Test rig in two different views*

Appendix 3: Control box for Vacon frequency variable drive and Festo servo drive

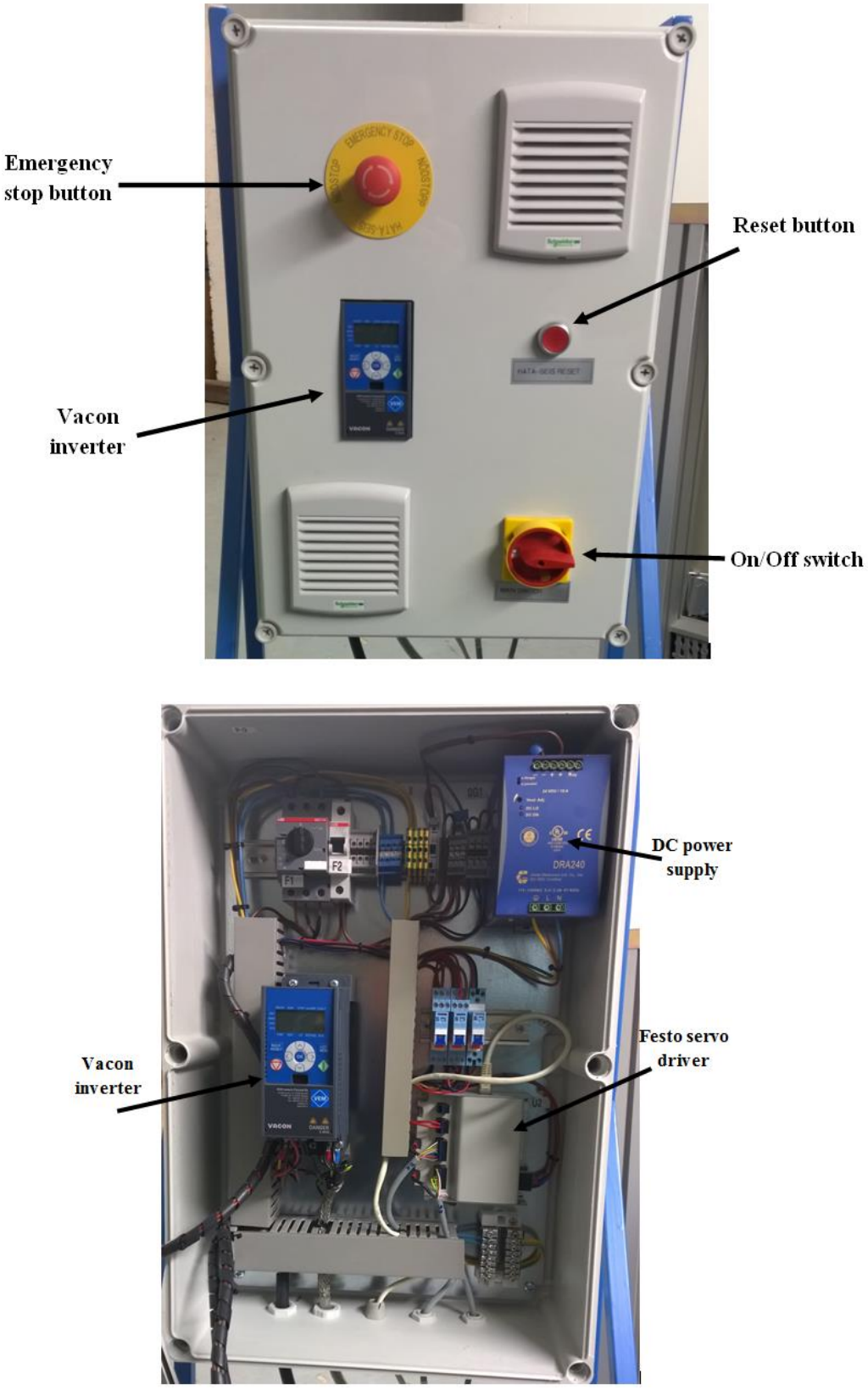

Figure 8.3 *Control box for Vacon frequency variable drive and Festo servo drive*